ORIGINAL PAPER

Ni^{2+} removal by ion exchange resins and activated carbon: a benchtop NMR study

M. Bernardi[1] · A.-L. Hantson[2] · G. Caulier[3] · S. Eyley[4] · W. Thielemans[4] · G. De Weireld[5] · Y. Gossuin[1]

Abstract

Heavy metal pollution in water is a critical environmental concern, demanding effective remediation techniques. Traditional methods, including ion exchange and adsorption, often rely on inductively coupled plasma (ICP) atomic emission spectroscopy/mass spectrometry (AES/MS) for the indirect and time-consuming measurement of residual metal concentrations. In contrast, this study employs innovative direct monitoring of nickel removal by benchtop NMR relaxometry using the paramagnetic properties of Ni^{2+}. To prove the feasibility of the NMR follow-up of Ni^{2+} uptake, batch experiments were performed with Amberlite IR120, Amberlite IRC748, Dowex Marathon MSC, and activated carbon (AC), which were previously characterized by various techniques. The effect of contact time, pH, and Ni^{2+} concentration on removal efficiency were studied. Pseudo-first and pseudo-second order kinetic models were used. The Langmuir model effectively described the equilibrium isotherms. The longitudinal and transverse relaxation curves of the loaded resins were biexponential. For sulfonic resins, a strong correlation was observed between the relaxation rates of the fast-relaxing fraction and the Ni^{2+} content determined by ICP-AES/MS. For IRC748, the effect of Ni^{2+} loading on the relaxation rates was weaker because of Ni^{2+} complexation. The relaxation curves of loaded AC revealed multiple fractions. Centrifugation was employed to eliminate the contribution of intergranular water. The remaining intragranular water contribution was biexponential. For high Ni^{2+} loadings, the relaxation rates of the slow relaxing fraction increased with the AC Ni^{2+} content. These results mark the initial stage in developing a column experiment to monitor, in real-time, adsorbent loading by NMR relaxometry.

Keywords NMR relaxometry · Nickel · Ion exchange resin · Activated carbon · Adsorption · Paramagnetic ion

Introduction

In recent years, water pollution by heavy metals, often caused by human activity, has become a major public concern (Akpor 2014; Sharma 2014; Tchounwou et al. 2012; Zamora-Ledezma et al. 2021). Without appropriate water treatment, heavy metal pollution can lead to disastrous consequences at the ecological level (He et al. 2005) and also has an impact on human health (Briffa et al. 2020). Indeed, many studies have demonstrated the correlation between heavy metal poisoning and cellular, DNA and nervous system damage (Azeh Engwa et al. 2019; Goyer and Clarkson 1996).

In order to remove heavy metals from water, various solutions have been implemented, such as flocculation, coagulation, precipitation, ion exchange and adsorption, each with its own advantages and disadvantages (Alyüz and Veli 2009; Burakov et al. 2018; Charerntanyarak 1999; Karnib et al. 2014; Qasem et al. 2021; Rajendran et al.

Editorial responsibility: Samareh Mirkia.

✉ Y. Gossuin
yves.gossuin@umons.ac.be

1 Biomedical Physics Unit, Research Institute for Materials Science and Engineering, UMONS, 25 Avenue Maistriau, 7000 Mons, Belgium

2 Chemical and Biochemical Process Engineering Unit, UMONS, 56 Rue de l'Epargne, 7000 Mons, Belgium

3 Biology of Marine Organisms and Biomimetics Unit, Research Institute for Biosciences, UMONS, 6 Avenue du Champ de Mars, 7000 Mons, Belgium

4 Sustainable Materials Lab, Chemical Engineering, KU Leuven, Kulak Kortrijk Campus, 53 E. Sabbelaan, 8500 Kortrijk, Belgium

5 Thermodynamic and Mathematical Physics Unit, UMONS, 31 Boulevard Dolez, 7000 Mons, Belgium

2022). Currently, the resin/adsorbent efficiency is generally evaluated through batch or column experiments, followed by atomic absorption/emission spectroscopy (AAS/AES) on the supernatant for the batch experiments and on the outlet effluent for the column experiments. However, this technique is indirect and generally requires an acid digestion of the sample prior to the spectroscopic analysis. It is therefore not suited for an in situ use to monitor resin saturation. Such an in situ control could avoid the packed bed being replaced too late (after it has reached its total exchange capacity) or too early (before it is sufficiently loaded). In this context, a non-destructive method to follow the breakthrough curve in real time would be really valuable.

Some heavy metals, such as Cr^{3+}, Cu^{2+}, Ni^{2+} and Mn^{2+} have paramagnetic properties and present a non-null magnetic moment. For instance, the magnetic moment of Ni^{2+} is $\mu_{Ni} = 3.88\ \mu_B$, where $\mu_B = 9.274 \times 10^{-24}$ J T^{-1} is the Bohr magneton. Proton nuclear magnetic resonance (NMR) can be used to detect these ions in aqueous solutions (Kock and Colnago 2022; Kock et al. 2018). Indeed, the presence of paramagnetic ions in water accelerates the water protons' NMR relaxation process which leads to a reduction of the transverse and longitudinal relaxation times T_1 and T_2. In the literature, several studies have reported the use of magnetic resonance imaging (MRI) to follow the migration, diffusion or adsorption of paramagnetic ions in different porous media (Bartacek et al. 2016; Moradi et al. 2008; Nestle et al. 2003). More recently, Gossuin and Vuong (2018), Gossuin et al. (2020) proposed to use benchtop NMR relaxometry, i.e., the measurement of water proton relaxation times, to follow the removal of paramagnetic ions (Cu^{2+} and Cr^{3+}) from water by alumina and an ion exchange resin (Amberlite IR120). NMR relaxometry is indeed much cheaper and easier to implement than MRI. The emergence of low field and "low cost" NMR could ease the use of relaxometry to follow the breakthrough curve of a sorbent in real time, which is not possible with conventional spectroscopic techniques (Michal 2020). Therefore, the aim of this study is to demonstrate the ability of NMR to monitor Ni^{2+} depollution using ion exchange resins and activated carbon, in order to pave the way for future real-time depollution monitoring.

In this work, the same method as in Gossuin et al. (2020) will be used to study the removal of another paramagnetic ion, Ni^{2+}, by three new adsorbents in addition to Amberlite IR120. We will start by characterizing the sorbent before focusing on the kinetics of adsorption by studying the influence of agitation time. We will also investigate the effect of metal ion concentration and pH on ion exchange/adsorption. Finally, we will correlate the relaxation times of the loaded resin/carbon with the metal content measured by inductively coupled plasma (ICP) atomic emission spectroscopy (AES) or mass spectrometry (MS). The results obtained in this work will first provide interesting data about the Ni^{2+} ion exchange/adsorption, like kinetics curves and isotherms, and they will also help to identify the strengths and weaknesses of the NMR relaxometry method. The research was conducted in Mons (Belgium) from March 2019 to December 2023.

Materials and methods

Samples

Two strongly acidic cation exchange resins [Amberlite IR120 and Dowex Marathon MSC (Sigma-Aldrich)] and one weakly acidic cation exchange resin [Amberlite IRC748 (Thermo Scientific Chemicals)] were investigated. The resins, whose main characteristics are given in Table 1, were selected on the basis of their structure (gel or macroporous) and their functional group (sulfonic or iminodiacetic group), which has a high affinity for heavy metal removal, and in particular, for nickel depollution (Silva et al. 2018). For the kinetic and isotherm experiments, the resin was used in its hydrated form. The weight of resin is therefore expressed in g of "wet" resin. For the study of the loaded resin relaxation properties, the resin was first loaded with Ni^{2+}, then dried and separated into two sets: one for Ni^{2+} quantification and the second for NMR experiments after rehydration. For these

Table 1 Physico-chemical properties of studied resins

	Amberlite IR120	Amberlite IRC748	Dowex Marathon MSC
Matrix	Styrene–divinylbenzene (DVB)	Macroporous styrene-DVB	Macroporous styrene-DVB
Functional group	Sulphonic acid	Iminodiacetic acid	Sulphonic acid
Ionic form	Na$^+$	Na$^+$	H$^+$
Particle size	0.60–0.80 mm	0.50–0.65 mm	0.525–0.625 mm
Moisture	40–50%	60–65%	50–56%
total exchange capacity	≥ 2.00 eq/L	≥ 1.35 eq/L	1.60 eq/L

experiments, the weight is therefore expressed in g of "dry" resin. The resins were used without further purification.

The commercial activated carbon (AC) used in this study was Darco® granular activated charcoal, 20–40 mesh particle size (Sigma-Aldrich). Prior to use, the material was reactivated by heat treatment at 650 °C in an inert atmosphere in order to increase its specific surface area, as previously reported by Yin et al. (2007) for various activation temperatures.

Filtration by centrifugation of the loaded resin/AC samples was carried out using an IEC CL31R Multispeed centrifuge (Thermo Scientific) at 5000 rpm for 2 min.

The solutions of Ni^{2+} were obtained by dissolving nickel nitrate hexahydrate in deionized water. The study of the effect of pH and agitation time were carried out with 50 mM Ni^{2+} solutions. The pH was adjusted by adding small amounts of concentrated NaOH and HCl solutions. All reagents were purchased from Sigma-Aldrich.

For the sake of conciseness, the terms "adsorbent", "sorbent" and "sorb" will be used to refer to the activated carbon and also to the resins, while it is clear that the ion-exchange process is not an adsorption process.

Characterization

The functional group of each adsorbent was determined using Fourier-transform infrared (FTIR) spectroscopy in attenuated total reflection (ATR) mode with a FTIR-8400 S (Shimadzu). Raman spectra were measured at room temperature on a SENTERRA spectrometer (Bruker). The instrument includes a monochromator, a filter system and a thermo-electrically cooled charge-coupled device (CCD). Continuous wave laser energy, at a wavelength of 532 nm (AC samples) or 785 nm (resin samples), was used as the excitation source. XPS measurements were performed on a Kratos Axis Supra photoelectron spectrometer, employing a monochromated Al Kα (1468.7 eV, 150 W) X-ray source and hemisphere analyzer. The analyzer was operated in fixed analyzer transmission (FAT) mode with survey spectra taken at a pass energy of 160 eV and high-resolution spectra at a pass energy of 40 eV. An aperture defined 110 μm analysis area was used for all analysis positions, and all spectra were acquired under charge neutralizing conditions, using a low energy electron gun within the field of the magnetic lens. The binding energy scale was charge referenced to aromatic carbon at 284.7 eV for the ion-exchange resin samples and graphitic carbon at 284.5 eV for the activated carbon samples. The instrumental transmission function was determined using the methodology developed at the National Physical Laboratory (NPL, UK) (Seah 1995). Spectra were processed in CasaXPS version 2.3.26rev1.2Q. Peak areas were converted into elemental composition using relative sensitivity factors based on Scofield cross sections,

corrected for the angular distribution of photoelectrons (for a source-analyzer angle of 60°) and the electron attenuation length according to Seah (2012). The resulting elemental composition does not consider nanostructure of the surface and should be considered the homogeneous equivalent composition. Sorbent morphology was analyzed by scanning electron microscopy (SEM) with a JSM-7200F Schottky Field Emission Scanning Electron Microscope (JEOL). Energy-dispersive X-ray (X-Max 80 EDS detector, Oxford Instruments) imaging was carried out to obtain a semi-quantitative analysis of the adsorbent composition. The X-rays are generated in a region of about 1–2 μm in depth. Activated carbon samples were gold–palladium coated prior to SEM/EDX analysis. The specific surface area of the carbon sample was obtained by the Brunauer Emmett and Teller (BET) method (Thommes et al. 2015) using a surface analyzer Belsorp Max with nitrogen gas as the adsorbate. Prior to measurements, the carbon samples were outgassed at 150 °C for 12 h. The mesopore volume (V_{meso}) and the mesopore surface (S_{meso}) were calculated using the BJH model (Lowell et al. 2004), and the micropore volume was obtained by subtracting the mesopore volume from the total pore volume.

Atomic emission spectroscopy

The samples were digested with a mixture of HNO_3–H_2O_2 (resins)/HNO_3–HCl (AC) in a microwave oven (Start D, Milestone or Multiwave 7000, Antoon Paar) prior to analysis. The standard solutions were prepared with the same proportion of HNO_3 to avoid matrix effects. The digested samples and standard solutions were analyzed by ICP-AES (Iris Intrepid II, Thermo Fischer Scientific) or ICP-MS (iCAP-q, Thermo Fischer Scientific).

NMR relaxometry

The relaxometric study of Ni^{2+} adsorption kinetics and the study of the relaxation properties of the Ni^{2+} loaded resins and AC were carried out on a homemade relaxometer composed of a 0.47 T (or 0.23 T for the macroporous resins) magnet coupled to a lapNMR console (Tecmag) and an RF power amplifier (Tomco). For Amberlite IR120, the influence of pH and initial Ni^{2+} concentration was studied with a Spintrack relaxometer (Process NMR) at a field of 0.68 T. For the other adsorbents, these measurements were made at 0.47 T. The choice of the magnetic field was made based on the amount of sample available and the range of relaxation times to measure. The weak dependance of the Ni^{2+} relaxivities with the field was taken into account and r_1 and r_2 were measured for each field (Table S1) and included in the calculations of the amount of captured Ni^{2+} (Eqs. 1 and 2). The relative error on the relaxation time

measurement is less than 4%. All experiments were carried out at room temperature.

For kinetics experiments, the measurement of the transverse relaxation time (T_2) was performed with a CPMG sequence, where the echo train covered a time interval of $\sim 3T_2$ with an interecho time ranging between 0.5 and 1 ms depending on the estimated T_2 value. For all experiments, the repetition time was taken as $5T_1$. For the experiments using the longitudinal relaxation of the solutions, the saturation recovery (SR) sequence was used to measure the longitudinal relaxation time (T_1). In this case, T_1 was preferred to T_2 for which an influence of the echo time on the results could have been a problem, especially for long T_2. The list of time delays was chosen to cover a time interval ranging from $\sim 0.2T_1$ to $5T_1$.

For the study of the relaxation properties of the loaded resin, the inversion recovery (IR) sequence was used with a list of time delays chosen to cover the whole T_1 relaxation curve, including very short delays to catch the fast initial relaxation. T_2 measurements were performed with a CPMG sequence and an interecho time ranging between 0.3 and 3 ms. The interecho time was chosen in order to cover the transverse relaxation curve of the fraction of interest.

Kinetics

Experimental procedure

To study the adsorption kinetics, an NMR tube was filled with 10 mg of wet resin or 50 mg of commercial AC and 350 μl of a 50 mM Ni^{2+} solution before being shaken by a vortex mixer at 500 rpm. At different time intervals, the sample was removed from the vortex mixer, introduced in the magnet and the transverse relaxation time T_2 was measured. After the NMR measurement, the sample was immediately put back under agitation. T_2 was chosen due to the shorter acquisition time (less than 15 s) when compared to T_1 (several minutes). The experimental set-up is shown in Fig. 1.

Interpretation of kinetic data

At the beginning of the experiment, the presence of paramagnetic Ni^{2+} ions in the solution leads to a short T_2 relaxation time which will progressively increase as these ions are captured. The relationship between the paramagnetic ion concentration and the solution relaxation rate is given by:

$$1/T_2^{ion} = 1/T_2^{water} + r_2 C \tag{1}$$

where T_2^{water} is the relaxation time of water in s^{-1}, r_2 is the transverse relaxivity in $s^{-1}\,mM^{-1}$ and C is the concentration of the paramagnetic ion in mM. The transverse relaxation time was measured at different time intervals, which allowed the monitoring of ion exchange/adsorption. At 0.68 T and at room temperature, the measured transverse relaxivity obtained for Ni^{2+} was 0.64 $s^{-1}\,mM^{-1}$ (Table S1), which is in good agreement with literature data (Bertini et al. 2005). T_2^{water} at 0.68 T and 20 °C is 2.0 s. The amount of metal adsorbed on the adsorbent is given by:

$$q = \frac{VA}{m}[C_0 - C] \tag{2}$$

where q is the amount of metal ion captured by the sorbent per gram of adsorbent expressed in $mg_{Ni}\,g_{sorb}^{-1}$; A is the atomic weight of Ni^{2+}; V is the volume of the solution in L; m is the mass of adsorbent in g and C_0 is the initial concentration of nickel in the solution in mM.

Many different kinetic models (e.g., pseudo-first order, pseudo-second order, Elovich, intraparticle diffusion) can be found in the literature among which the most used are the pseudo-first-order (Lagergren equation) and the pseudo-second-order models (Gautam et al. 2014; Ho and McKay 1998).

The pseudo-first-order kinetic model predicts that:

$$q(t) = q_1(1 - e^{-k_1 t}) \tag{3}$$

Fig. 1 Kinetic experimental set-up
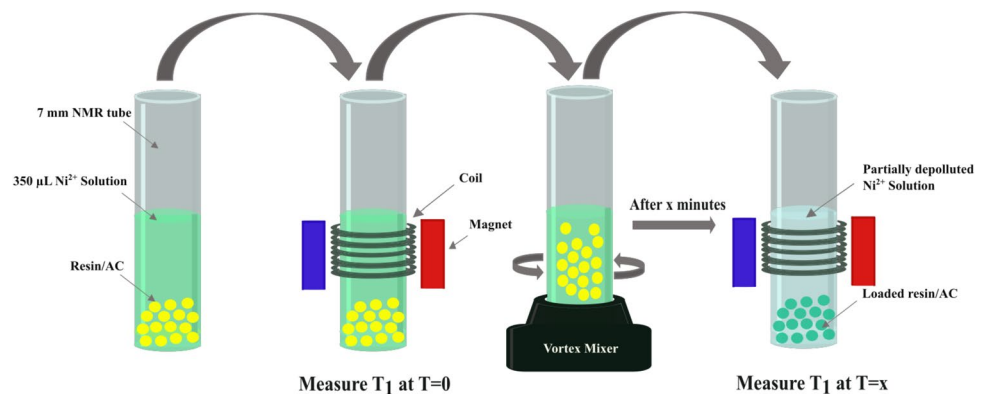
While in the pseudo-second-order model, $q(t)$ is expressed as:

$$q(t) = \frac{k_2 q_2^2 t}{1 + k_2 q_2 t} \tag{4}$$

where q_1 and q_2 are the amount of adsorbed metal at equilibrium in $mg_{Ni} \, g_{sorb}^{-1}$ obtained by the pseudo-first-order and pseudo-second-order models, respectively; k_1 is the first-order ion exchange/adsorption rate in min^{-1}; k_2 is the second order equilibrium rate constant expressed in $g_{sorb} \, mg_{Ni}^{-1} \, min^{-1}$.

Isotherms

Experimental procedure

For the isotherm experiments, a sample containing a given mass of adsorbent (5.5 mg of wet IR120 and Marathon MSC resin; 5 mg of wet IRC748 resin; 50 mg of commercial AC) was put in contact with a Ni^{2+} aqueous solution and shaken on an orbital shaker at 300 rpm until equilibrium was reached. The longitudinal relaxation time of the sample was then measured.

Interpretation of isotherm data

The longitudinal relaxation time allowed the equilibrium metal concentration of the solution and then the amount of metal captured by the resin/AC to be determined using Eqs. 1 and 2, as described in the previous section but with T_1 and r_1 instead of T_2 and r_2, respectively. The measured longitudinal relaxivity of Ni^{2+} was 0.60 and 0.56 $s^{-1} \, mM^{-1}$ at 0.47 and 0.68 T, respectively (Table S1). The experiment was repeated for several initial Ni^{2+} concentrations but always with the same amount of resin/AC. The obtained results were then analyzed with the Langmuir and Freundlich models (Gautam et al. 2014). To ease the comparison with literature, the Ni^{2+} concentrations are expressed in mg L^{-1} for the isotherm data.

The Langmuir isotherm equation is given by:

$$q_e = \frac{q_{max} K_L C_e}{1 + K_L C_e} \tag{5}$$

where q_{max} is the maximum adsorption capacity expressed in $mg_{Ni} \, g_{sorb}^{-1}$; K_L is the sorption equilibrium constant in L mg^{-1}; q_e is the equilibrium adsorption capacity in $mg_{Ni} \, g_{sorb}^{-1}$; C_e is the equilibrium concentration of Ni^{2+} remaining in solution in mg L^{-1}.

The Freundlich isotherm can be described by:

$$q_e = K_F C_e^{1/n} \tag{6}$$

where K_F is an adsorption capacity constant expressed in $mg_{Ni}^{1-1/n} \, g_{sorb}^{-1} \, L^{1/n}$ and n is the adsorption intensity.

Effect of pH

To investigate the effect of pH on Ni^{2+} removal, several solutions of Ni^{2+} were prepared at different pHs. The pH was adjusted by adding a small amount of NaOH or HCl. 350 µL of each solution was transferred to an NMR tube containing the resin/AC (10 mg of wet IR120 or wet Marathon MSC resin; 5 mg of wet IRC748 resin; 50 mg of commercial AC). The tubes were shaken at 300 rpm on an orbital shaker until the equilibrium was reached. After that, T_1 was measured, which allowed the equilibrium metal concentration of the solution and the amount of metal captured by the resin/AC to be determined, as previously described. For all experiments, T_1 of the initial Ni^{2+} solution was measured to investigate the influence of pH on the relaxation induced by Ni^{2+}. In the pH range studied, the longitudinal relaxation time of Ni^{2+} solutions was not affected by pH (Fig. S1). In this section, only initial pH values were taken into account. After adsorption or ion exchange, a change in pH can occur as reported by Kalak et al. (2021) after Cu^{2+} and Pb^{2+} adsorption by fly ash. However, the pH change observed was insufficient to induce precipitation of nickel hydroxide complexes.

Relaxation induced by the Ni^{2+} loaded resins/AC

Experimental procedure

To study the ion exchange/adsorption directly within the sorbent, adsorbents loaded with increasing amounts of Ni^{2+} were prepared: a given mass of adsorbent (1 g for Amberlite IR120 and AC; 10 g for Dowex Marathon MSC and Amberlite IRC748) and a fixed volume of Ni^{2+} solution (10 mL for Amberlite IR120; 25 mL for the other sorbents) were added to a beaker and shaken by a magnetic stirrer until the ion exchange/adsorption equilibrium was reached. To achieve different Ni^{2+} loadings of sorbents, the experiment was reproduced with different initial Ni^{2+} concentrations ranging from nickel-free solution to 100 mM Ni^{2+} solution. The sorbent/solution mixture was then rinsed with distilled water and filtered with filter paper to collect the loaded sorbent. Thereafter, the adsorbent was placed in an oven at 70 °C overnight. The next day, an NMR tube was filled with a
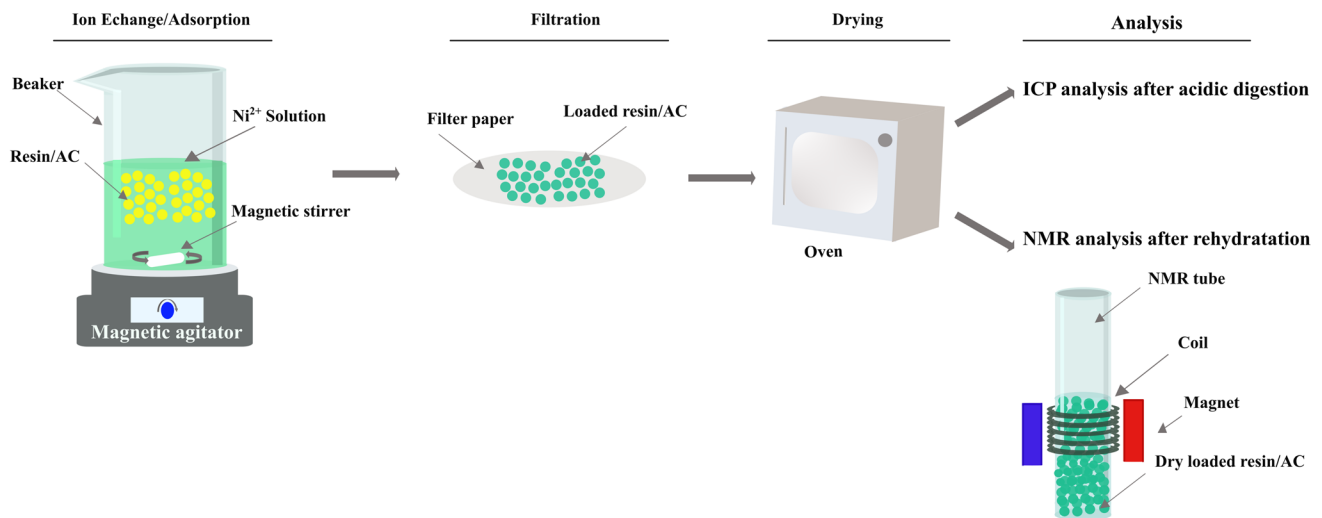
Fig. 2 Loaded resin/AC experimental set-up

small amount of dry resin/AC (200 mg for Amberlite IR120; 80 mg for AC; 2 g for Dowex Marathon MSC and 1.5 g Amberlite IRC748) and rehydrated with a given amount of distilled water chosen thanks to preliminary experiments (200 μL for Amberlite IR120 and AC; 4 mL for Dowex Marathon MSC and 4.3 mL for Amberlite IRC748). One hour after the preparation of the tube, the NMR relaxation properties of the sample were measured. The amount Ni^{2+} captured by the adsorbent was determined by ICP AES/MS analysis after digestion of a small amount of the Ni^{2+} loaded dry adsorbent. The experimental set-up is shown in Fig. 2.

Interpretation of the loaded resin/AC data

In porous media, T_1 and T_2 relaxation curves generally exhibit a multiexponential behavior, because there are several populations of protons presenting different relaxation times, which are related to the different porosities found in the system (Brownstein and Tarr 1979). Moreover, the relaxation rate of each population is composed of two (for T_1) or three contributions (for T_2). Indeed, the diffusion of the protons in the magnetic field gradients shortens T_2 but leaves T_1 unaffected. However, the contribution to the transverse relaxation of the diffusion in the magnetic field inhomogeneities is often neglected at low magnetic fields. Within this approximation, T_1 and T_2 are simply given by:

$$1/T_i = 1/T_i^{Bulk} + 1/T_i^{Surface} \tag{7}$$

where subscript i denotes 1 or 2 for T_1 and T_2, respectively; $1/T_i^{Bulk}$ is the bulk relaxation rate; $1/T_i^{Surface}$ is the surface relaxation rate (i.e., the relaxation time of the pore fluid influenced by the pore surface). $1/T_i^{Bulk}$ is usually much smaller than $1/T_i^{Surface}$ and the relaxation rates observed in a

single water filled pore can simply be related to the surface-to-volume ratio (S/V) of the pore by:

$$1/T_i \approx 1/T_i^{Surface} = \rho_i S/V \tag{8}$$

where ρ_i, the surface relaxivity, describes the capacity of the surface to accelerate the proton relaxation. This usually increases with the concentration of paramagnetic centers on a surface (Foley et al. 1996; Grunewald and Knight 2009).

Results and discussion

Characterization

Figure 3 shows the FTIR spectra of the adsorbents before and after Ni^{2+} loading, which are very similar. For all the adsorbents, peaks around 3375 cm^{-1} and 1630 cm^{-1}, related to the –OH stretching vibration, were observed. For the resins, the C–H stretching mode of the styrene polymeric matric was observed at approximately 2910 cm^{-1} (Jha et al. 2009). For the Amberlite IR120 and Dowex Marathon MSC, the functional sulfonate SO^{3-} groups involved in Ni^{2+} exchange were observed in the range of 1200–1000 cm^{-1} (El-Hamid et al. 2020). The characteristic bands for the iminodiacetate groups of the Amberlite IRC748 were found at 1750–1250 cm^{-1}: the stretching vibration of the C=O groups present in the carboxyl groups appeared at 1600 cm^{-1}, while protonated carboxyl groups (COO–) were observed at 1400 cm^{-1}. Finally, the peak at 1330 cm^{-1} is associated with the stretching vibrations of the C–O and C–N groups (Kołodyńska et al. 2020; Ling et al. 2010). Analysis of the activated carbon spectra shows peaks at 2350 cm^{-1} and 1620 cm^{-1}, which are related to O=C=O stretching due to
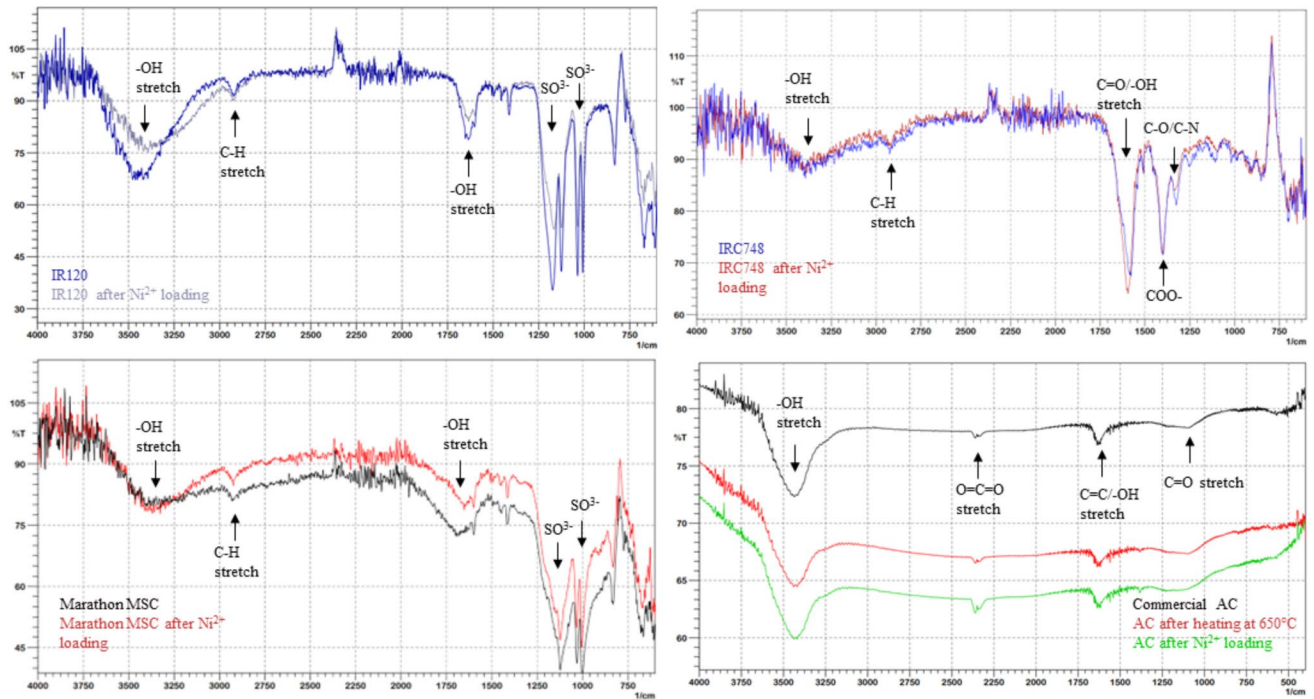
Fig. 3 Infrared spectra of adsorbents before and after adsorption of Ni^{2+} (dry form)
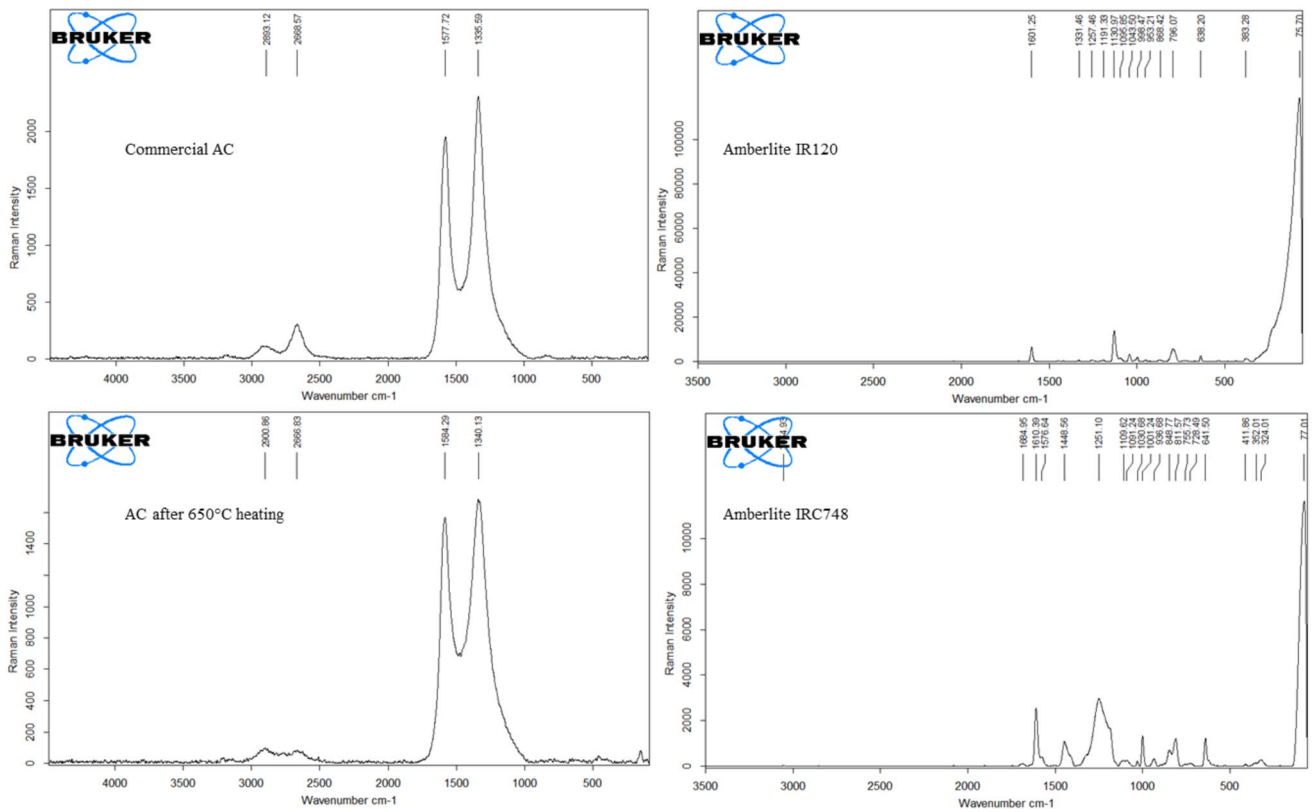

Fig. 4 Raman spectrum of adsorbents after baseline correction

atmospheric contamination and C=C stretching respectively (Shin et al. 1997; Yakout and Sharaf El-Deen 2016). A weak transmittance band around 1000–1200 cm^{-1} can be ascribed to C=O stretching (Park et al. 1997). The FTIR results show that the capture of Ni^{2+} by the resin/AC does not alter its chemical structure, especially its functional groups.

Figure 4 displays the Raman spectrum (4500–90 cm^{-1}) which was acquired for the AC, AC after thermal reactivation (AC 650 °C), Amberlite IR120 and Amberlite IRC748. Regarding the analysis of the charcoal samples, one important piece of information is the D to G ratio, which is well described in the literature (Katz et al. 2022; Thapliyal et al. 2022). The G band is related to graphitic phases (high order) of the material, while the D band relates to defects in the graphitic phases (low order). The characteristic D band for the AC and AC 650 °C was found at 1336 and 1340 cm^{-1}, respectively. The G band was observed at 1580 cm^{-1} (AC) and 1587 cm^{-1} (AC 650 °C). In addition to the D and G bands, other vibration modes correlated with crystal lattice disorder can be seen in Fig. 4. These include the D$_3$ band at 1464 cm^{-1} (AC); 1474 cm^{-1} (AC 650 °C), related to defects outside the aromatic layers, and the D$_4$ band around 1240 cm^{-1} attributed to disorder in the graphitic lattice (Ag symmetry) or ionic impurities (Katz et al. 2022; Thapliyal et al. 2022). Moreover, two distinct peaks found in the Raman spectra of AC before and after thermal activation can be assigned to combinations of the Raman fundamentals: the 2D band at 2670 cm^{-1} and the D + G band around 2900 cm^{-1}. The D/G ratio for the AC 1.51 before thermal activation and 1.12 after thermal activation. As this value is lower compared to values obtained for commercial AC, thermal activation leads to a higher proportion of ordered graphitic material. From Fig. 4, the C=CH and C=C stretching modes of the IR120 aromatic ring are found at 1601 cm^{-1} and 998 cm^{-1} respectively (Edwards et al. 2000; Larkin 2011). The peaks in the range of 1257–1096 cm^{-1} are assigned to S–O stretching for the IR120 resin (Larkin

2011). Presence of the peak at 1044 cm^{-1} can be attributed to stretching of S–O or the specific ring vibration of the aromatic ring. S–C stretching is found at 796 cm^{-1} (Edwards et al. 2000; Larkin 2011). Finally, the deformation of SO$_3$ is observed at 638 cm^{-1}, this peak can also be attributed to the specific ring vibration of the IR120 aromatic ring. For the IRC748 resin. The C=CH stretching mode of the styrene DVB matrix is observed at 1610 cm^{-1} (Fig. 4). The other peaks due to the aromatic ring are found in the region of 1091–1001 cm^{-1} and 849–324 cm^{-1} (Larkin 2011). The peak present at 1577 cm^{-1} may be assigned to either NH deformation or C=CH stretching. The iminodiacetate functional groups of the IRC748 resin are observed at 1685 cm^{-1} (stretching of C=O), 1449 cm^{-1} (stretching of C–C), 1251 cm^{-1} (stretching of C–O) and 1110 cm^{-1} (stretching of C–N) (Vijayan et al. 2013) VI. The Raman band for the resin Dowex Marathon MSC sample are expected to be similar to the Amberlite IR120 because they differ only by their physico-chemical state and counterion: macroporous for the Dowex resin (H$^+$) and gel type for the IR120 resin (Na$^+$). However, no Raman bands could be obtained for the Dowex resin due to excessive fluorescence. Neither 785 nm nor 582 nm excitation, gave rise to a usable Raman spectrum.

XPS was used to probe the surface composition of the samples. The elemental composition derived from the survey spectra is given in Table 2. Nickel was detected on all the Ni^{2+} loaded AC and resins, except on Dowex Marathon MSC, for which no Ni was detectable in the XPS, suggesting that either the loading was below the detection limit, or the Ni was deposited beneath the surface of the beads. For IR120 and IRC748, there was still a significant quantity of sodium detected in the nickel samples, suggesting incomplete loading with nickel, as expected. Indeed, samples used for XPS quantification are not fully saturated. Furthermore, there is a disparity in the M:S (0.5:1 instead of 1:1 for IR120) and M:N (1.5:1 instead of 2:1 for IRC748) ratios, which could indicate the presence of H+ as the counterion,

Table 2 Elemental composition from XPS spectra

|	Equivalent homogeneous concentration/at%								
	Al 2s	C 1s	Cl 2p	N 1s	Na 1s	Ni 2p3/2	O 1s	S 2p	Si 2p
AC	0.42 ± 0.73	87.14 ± 4.97					9.3 ± 2.8	0.32 ± 0.05	2.81 ± 1.4
AC after heating at 650 °C	0.22 ± 0.38	90.95 ± 2.53					6.69 ± 1.28	0.28 ± 0.02	1.87 ± 0.87
AC + Ni		86.48 ± 1.98				1.95 ± 0.53	10.19 ± 1.45	0.18 ± 0.05	1.2 ± 0.28
Marathon MSC		67.48 ± 0.78	0.78 ± 0.73				22.66 ± 0.15	9.08 ± 0.25	
Marathon MSC + Ni		67.65 ± 0.33	0.37 ± 0.15				22.61 ± 0.26	9.36 ± 0.2	
IR120		65.12 ± 2.02			6.54 ± 1.68		20.55 ± 0.9	7.8 ± 0.27	
IR120 + Ni		71.56 ± 0.98	0.61 ± 0.53		1.64 ± 0.21	1.11 ± 0.22	19.59 ± 0.71	5.49 ± 0.46	
IRC748		70.05 ± 2.15	0.22 ± 0.11	3.99 ± 0.19	9.28 ± 1.42		16.44 ± 0.87		
IRC748 + Ni		66.66 ± 3.33	0.09 ± 0.09	4.71 ± 0.48	6.18 ± 0.17	0.78 ± 0.57	21.59 ± 3.73		
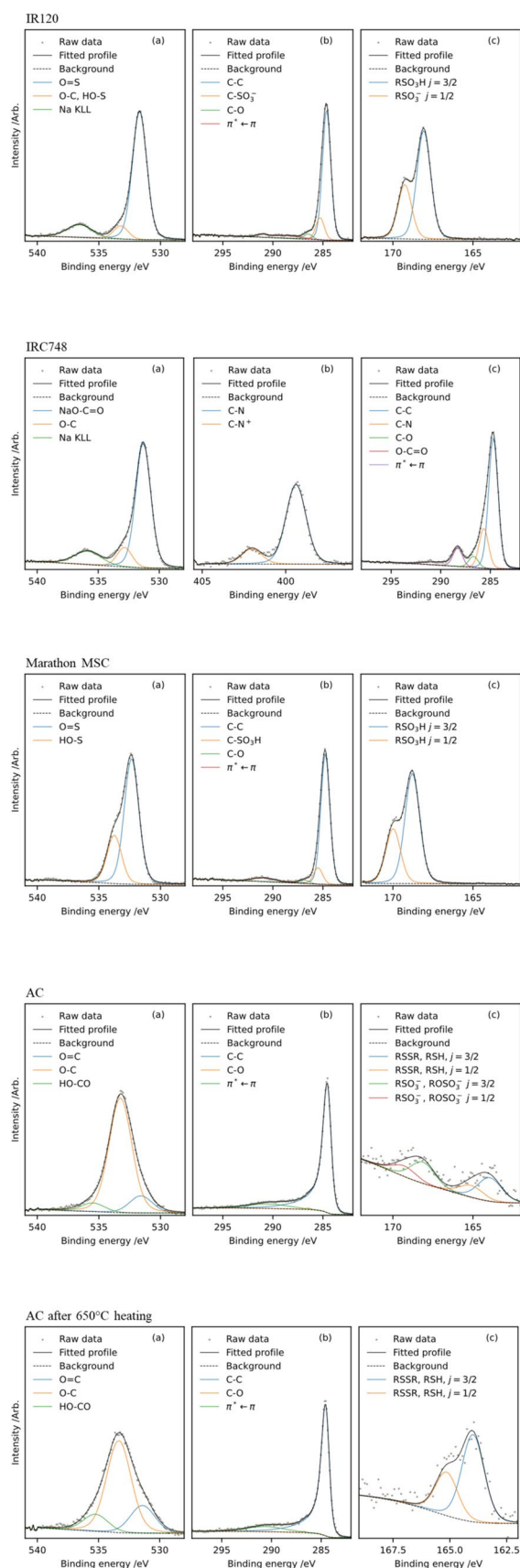
Fig. 5 O1*s* (**a**), C1*s* (**b**) and S2*p* (**c**) XPS spectra of adsorbents

which is undetectable by XPS. Figure 5 displays the XPS spectra of adsorbents for O1*s* (a), C1*s* (b), and S2*p* (c), while Table S2 summarizes the binding energies of these spectra. From Fig. 5 and Table S2, the high-resolution carbon 1*s* spectra of the sulfonate resins showed three carbon environments, corresponding with C–C (284.7 eV), C–SO$_3$ (285.3–285.6 eV) and C–O (286.5–286.9 eV) environments (Beamson and Briggs 2000). The latter small contribution is likely due to impurities on the surface of the samples. There are also small, broad contributions at higher binding energy that can be assigned to $\pi^* \leftarrow \pi$ shake-up events due to the aromatic nature of the sample. These assignments are supported by the oxygen 1*s* spectra, which show two oxygen environments at 531.7–532.3 eV and 533.2–533.7 eV corresponding with S=O/S–O– and C–OH/S–OH respectively. The difference in counter-ion between IR120 and Dowex Marathon MSC is visible from the overlapping Na KLL Auger peak at 950 eV kinetic energy (appearing at 536.6 eV on the binding energy scale) in the former and the increased intensity of the peak at 533.7 eV due to S–OH contributions in the latter. This is also supported by the sulfur 2*p* spectra of the samples were there is a shift in the sulfur 2*p*3/2 binding energy from 168.8 eV in Dowex Marathon MSC to 168.1 eV in IR120, consistent with greater negative charge on the sulfonate group when paired with a sodium cation. The iminodiacetate resin IRC748 showed four environments in the carbon 1*s* spectrum, corresponding with C–C (284.7 eV), C–N (285.7 eV), C–O (286.7 eV) and carboxylate (288.3 eV), as well as the $\pi^* \leftarrow \pi$ shake-up contribution seen in the sulfonate resins as mentioned above. The oxygen 1*s* spectrum of this material showed a main component at 531.3 eV due to carboxylate functionalities, with a small C–O component at 532.8 eV, likely due to the same contamination seen in the carbon 1*s* spectrum (Fig. 5). The overlapping Na KLL Auger can also be seen at high binding energy. The nitrogen 1*s* spectrum reveals that while most of the nitrogen is present as an amine (399.4 eV), some quaternary species are present (402.0 eV), perhaps due to impurities from the synthesis of iminodiacetic acid or simply from protonation of the resin. The spectra of the activated carbon samples, both before and after activation are strikingly different from those of the resin samples. The carbon 1*s* spectra show an intense asymmetric component due to graphitic carbon at (284.5 eV) with satellite features due to excitation of delocalized electrons in the graphitic structure. This asymmetry causes difficulty in accurately assigning intensity on the high binding energy side of the peak to other carbon environments. There is only one small contribution at 286.5 eV (C–O), however, higher binding energy contributions due to, e.g., C=O or O–C=O may be covered by the tail of the *sp*2 C–C peak and or the shake-up satellite intensity. The presence of these functional groups is alluded to by the presence of two components in the oxygen 1*s* spectrum at 531.6 eV (O=C)

and 533.5 eV (HO–C), however, other contributions to the oxygen 1s spectrum involving different elements cannot be ruled out. The only difference in the chemistry of the two samples that is visible in the high-resolution spectra is the presence of two sulfur environments in AC and only one in the thermally reactivated sample. AC contained both high oxidation state sulfur (e.g. sulfonate) with an S 2p3/2 binding energy of 168.3 eV and low oxidation state sulfur (thiol, disulfide) with a binding energy of 163.9 eV, whereas AC 650 °C contains only the latter environment. For all samples, the adsorption of nickel did not result in noticeable changes in the carbon, oxygen, nitrogen, or sulfur spectra of the adsorbents (Fig. S2.). The Ni 2p spectra of all of the samples show 2p3/2 peak maxima around 855–856 eV, consistent with Ni(II) species (Biesinger et al. 2012), with no significant low-binding energy shoulders that could be indicative of NiO or Ni(0) presence in the sample (Biesinger et al. 2009) (Fig. 6 and Table S2). The Ni 2p spectra show complex multiplet splitting due to coupling of the unpaired core electron from photoionization with unpaired d-electrons (Fig. 6 and Table S2.). Relative to the other samples, there is a decreased intensity of the high binding energy multiplet peaks for IRC748, which likely indicates complexation by the iminodicarboxylate group on the resin as this intensity is known to vary with different ligand fields and is absent in low-spin complexes (Gupta and Sen 1975).

SEM images of the dry adsorbent before and after Ni^{2+} sorption are shown in Fig. 7. After Ni^{2+} capture, a change in the surface morphology can be observed with the appearance of large cracks on the surface of the IR120 resin, as
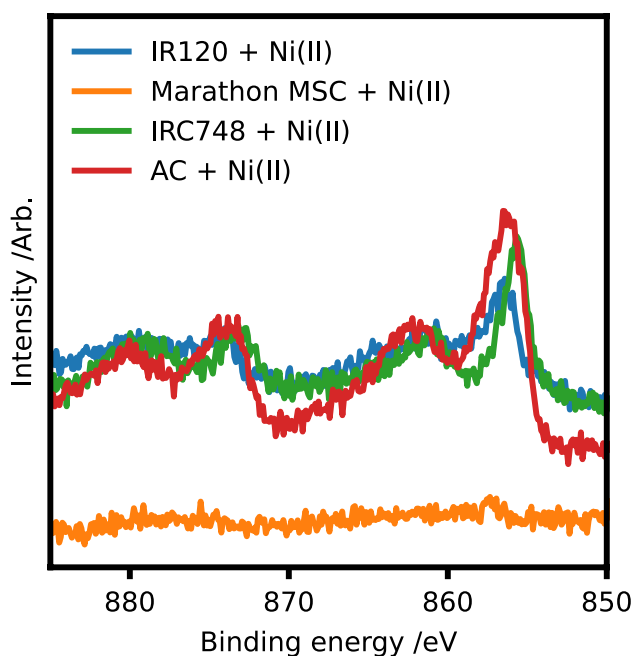
previously described (El-Hamid et al. 2020). Indeed, when the ion with its solvation shell penetrates the porous matrix, a swelling occurs due to the strong osmotic pressure, leading to the formation of cracks. Such cracks were not observed for the Ni^{2+} loaded Dowex Marathon and IRC748 resins. This is due to the macroporous structure of these resins, which results in lower osmotic pressures. SEM images of the activated carbon sample show an irregular and porous surface (Fig. 7), suggesting a high surface area, as confirmed by the BET analysis. Table 3 presents the characteristics of the activated carbon before and after the thermal reactivation, which causes an increase of nearly 25% in the BET specific surface area and more than 17% in the total pore volume. Thermal reactivation also increases the volume occupied by the micropores from 0.25 to 0.29%. The increase in the specific surface area of the activated carbon leads to the creation of additional adsorption sites and thus to an increase in sorption capacity. Table S3 shows a change in Ni^{2+} adsorption capacity for the experimental conditions studied (20 mg AC and 5 mM Ni^{2+} solution), from 1.1 to 5.03 mg_{Ni}/g_{AC} after thermal reactivation.

The EDX analysis confirmed the presence of Ni^{2+} on the surface of the resin/AC after the Ni^{2+} loading experiment (Table S4), while the original commercial adsorbents did not seem to contain any Ni.

However, ICP AES/MS analysis revealed the presence of a non-negligible amount of paramagnetic impurities in the AC before the metal impregnation: 1.6 mg/g_{AC} of Fe^{3+} and lower amounts (≈ 15–40 $\mu g/g_{AC}$) of other paramagnetic metals, such as Mn^{2+}, Cu^{2+}, Cr^{3+}. No paramagnetic impurities were detected for the three resins studied.

Kinetic study

Figure S3 shows the NMR monitoring of Ni^{2+} exchange on the Amberlite IR120 resin. The observable increase in T_2 over time is the result of the decrease in Ni^{2+} concentration in the solution, attributed to nickel capture by the resin. Using Eqs. 1 and 2, the amount of captured Ni^{2+} can be calculated. Figure 8 shows, for the four adsorbents, the increase of the amount of Ni^{2+} loaded on the resin/AC with time, until equilibrium was reached. In the case of ion exchange by the IR120 resin, the Ni^{2+} uptake was fast during the first minutes before finally reaching equilibrium after approximately 15 min of agitation (Fig. 8). The experiment was triplicated and showed good reproducibility. The ion exchange of Ni^{2+} on the Dowex Marathon MSC revealed the fastest kinetics, reaching equilibrium after 10 min, while the Amberlite IRC748 and AC showed slower kinetics with equilibrium reached after 30 min. The data were analyzed with the two kinetic models (Eqs. 3 and 4) and compared with previous results of Ni^{2+} removal by sulfonic/chelating resin or AC. Both kinetic models fitted the experimental
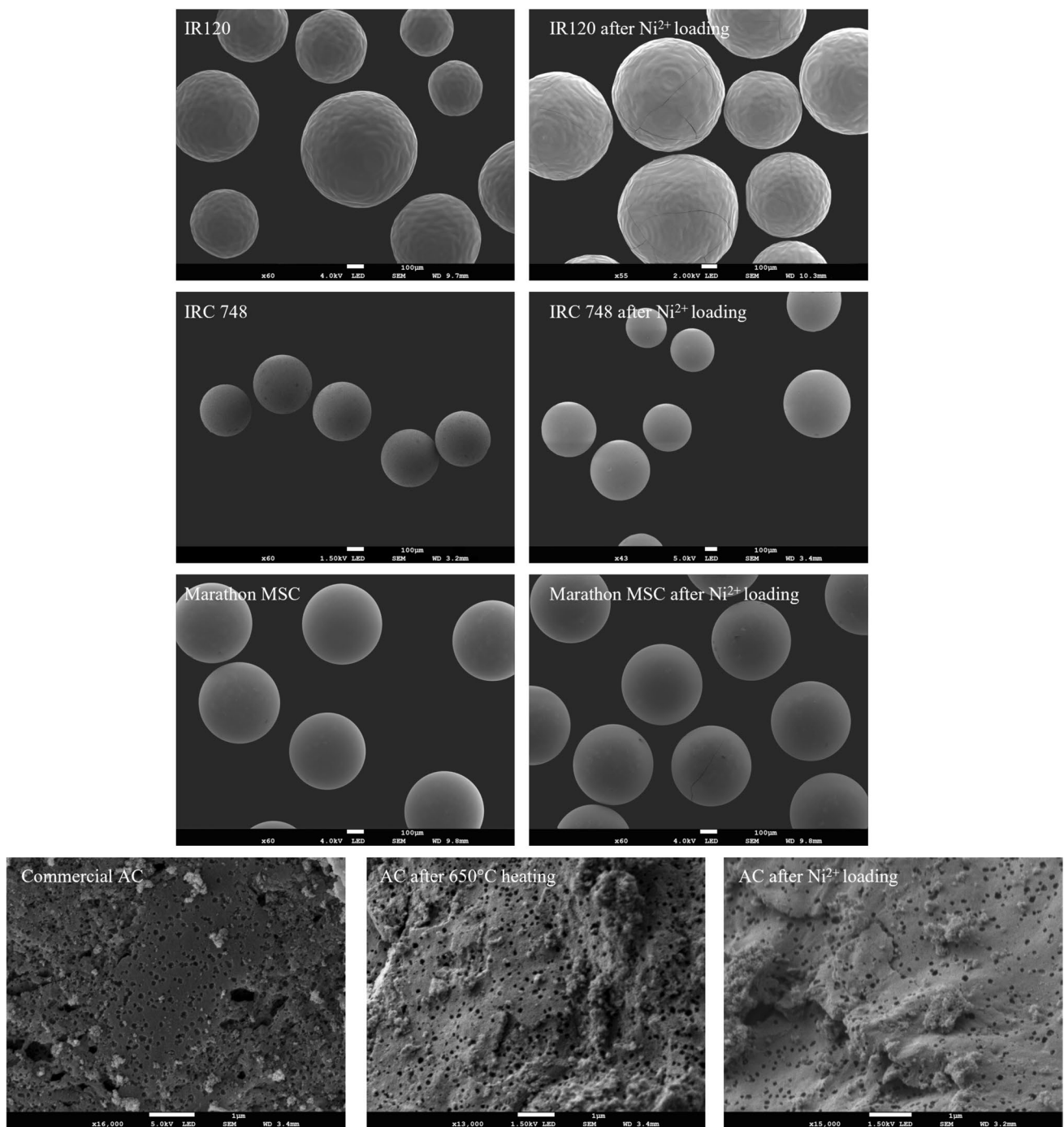

Fig. 6 Ni 2p XPS spectra of adsorbents

Fig. 7 SEM micrographs of adsorbents before and after Ni^{2+} sorption

Table 3 Parameters of the AC porous structure calculated from the adsorption isotherms of nitrogen vapor at 77 K

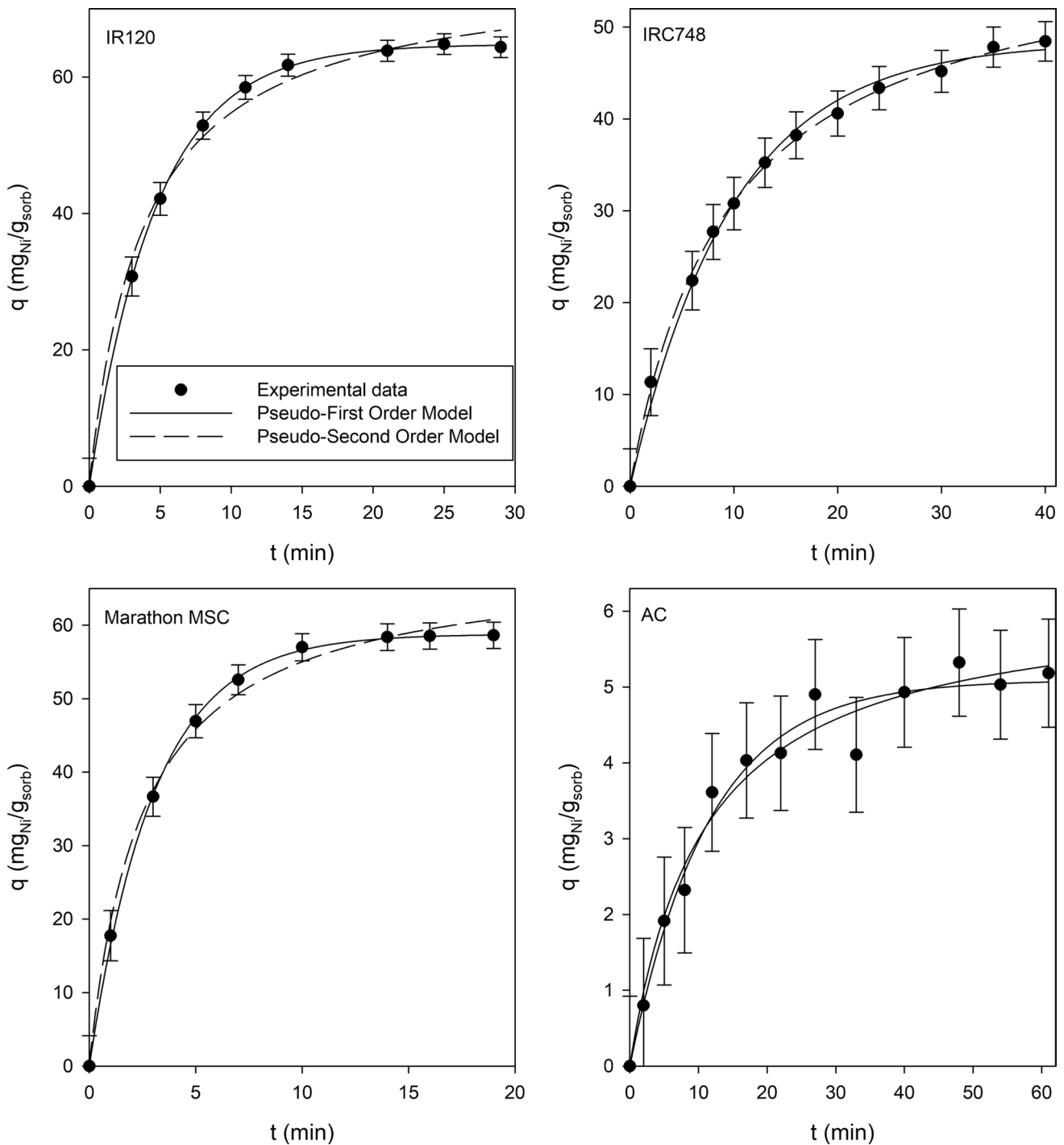|	S_{BET} (m^2 g^{-1})	S_{meso} (m^2 g^{-1})	Total pore volume (cm^3 g^{-1})	V_{micro} (cm^3 g^{-1})	V_{meso} (cm^3 g^{-1})	V_{micro}/V_{total} (%)
AC	556.16	223.27	0.67	0.17	0.5	0.25
AC after heating at 650 °C	693.68	246.45	0.79	0.23	0.56	0.29

Fig. 8 Fitting of the kinetics data with a pseudo-first- and pseudo-second order model for Ni^{2+} removal by resin/AC

data well (Fig. 8). However, for all adsorbents, except the IRC748 resin, the correlation coefficient R^2 obtained with the first order model was larger (Table 4). The activated carbon presented a much lower adsorption capacity than the resins: AC < IRC748 < Marathon MSC < IR120 (Table 4). For the activated carbon, the kinetic parameters obtained

were in a rather good agreement with the published data, especially with the parameters obtained by Lata et al. (2008) and Wang et al. (2010). The values of q_1 and q_2 obtained for the studied resins are close to those previously reported for similar resins (Alyüz and Veli 2009; Dizge et al. 2009). The obtained pseudo-first-order and pseudo-second-order

Table 4 Parameters of pseudo-first-, pseudo-second-order kinetic model. Comparison with literature data

| Adsorbent	T (°C)	pH	Pseudo first order			Pseudo second order			References
			q_1 (mg$_{Ni}$/g$_{sorb}$)	k_1 (min^{-1})	R^2	q_2 (mg$_{Ni}$/g$_{sorb}$)	k_2 (g$_{sorb}$ mg$_{Ni}^{-1}$ min^{-1})	R^2	
Activated charcoal	22	4.5	5.09 ± 0.15	$(87.4 \pm 9) \times 10^{-3}$	0.98	6.2 ± 0.3	$(15.1 \pm 3.1) \times 10^{-3}$	0.97	This study
Dowex Marathon MSC H+wet	22	4.5	58.8 ± 0.31	$(330 \pm 7) \times 10^{-3}$	1.00	68.8 ± 1.6	$(58 \pm 0.7) \times 10^{-3}$	0.99	This study
Amberlite IRC748 Na+wet	20	4.5	48.4 ± 0.7	$(101.6 \pm 4.2) \times 10^{-3}$	1.00	60.0 ± 0.6	$(180 \pm 7) \times 10^{-5}$	1.00	This study
Amberlite IR120 Na+wet	22	4.5	64.78 ± 0.14	$(212 \pm 1.7) \times 10^{-3}$	1.00	75.6 ± 2	$(35 \pm 4)10^{-3}$	0.99	This study
Amberlite IR120 H$^+$	45	/	0.38	0.12	0.96	500	1.6×10^{-4}	0.99	Fatima et al. (2020)
Dowex HCR S/S	23	4	38.8	4.8×10^{-2}	/	50.8	3.5×10^{-3}	/	Alyüz and Veli (2009)
Lewatit monoplus SP 112 H+dry	25	6	42.3	4×10^{-2}	/	55.2	1.3×10^{-3}	/	Dizge et al. (2009)
Amberlite IRN77 H+	25	4.8	/	0.98	/	/	/	/	Rengaraj et al. (2002)
Dowex C400	20	5	/	1.4×10^{-2}	/	/	4.9×10^{-4}	/	Alguacil (2017)
Amberlite IR120 H+dry	20	/	5.7	8×10^{-4}	0.92	11.4	3.2×10^{-4}	0.99	Ates and Basak (2021)
Lewatit TP207 Na+dry	20	/	5.44	9.8×10^{-4}	0.94	11	3.2×10^{-4}	0.99	Ates and Basak (2021)
Purolite C100-MB H+dry	20	5.5	/	4.2×10^{-2}	0.93	/	0.26	0.91	Amin et al. (2015)
TP220	25	/	5.2	2.75	0.91	5.31	1.22	0.93	Wołowicz and Wawrzkiewicz (2021)
Activated carbon (peanut hulls)	30	5	/	2.9×10^{-2}*	/	/	/	/	Periasamy and Namasivayam (1995)
Granular activated carbon	30	5	/	1.2×10^{-2}*	/	/	/	/	Periasamy and Namasivayam (1995)
Activated carbon (coconut shell)	25	5.8	11.6	1.9×10^{-2}	0.99	30.5	1655.5	1.00	Moreno-Piraján et al. (2011)
Activated carbon (Mespilus germanica leaves)	25	7	23.28	0.1	0.94	75	6.9	1.00	Khedri et al. (2022)
Activated carbon (walnut shell)	30	6	14.5	4×10^{-2}*	0.97	14.47	2.7×10^{-2}	1.00	Wang et al. (2010)
Activated carbon (Parthenium hysterophorus L)	23	5	4	1.6×10^{-2}	0.99	9.9	10^{-2}	1.00	Lata et al. (2008)

*k_1 parameter is divided by a factor of 2.303 in these references

rates seem to be larger than expected from the literature data (Alguacil 2017; Ates and Basak 2021). However, these parameters are strongly dependent on the experimental conditions, such as the initial metal concentration, the volume of the treated solution, the amount of resin, the speed of agitation and the condition of the resin (wet or dry), which could explain this difference. Table 4 only reports the results of the analysis of the kinetic data with the pseudo-first-, and second-order models which in our case provide good correlation coefficients. It should be mentioned, however, that other models were already used in the literature to describe the kinetics of Ni^{2+} uptake by adsorbents, such as Elovich

Fig. 9 Effect of pH on the Ni^{2+} exchange/adsorption efficiency of resins/AC studied
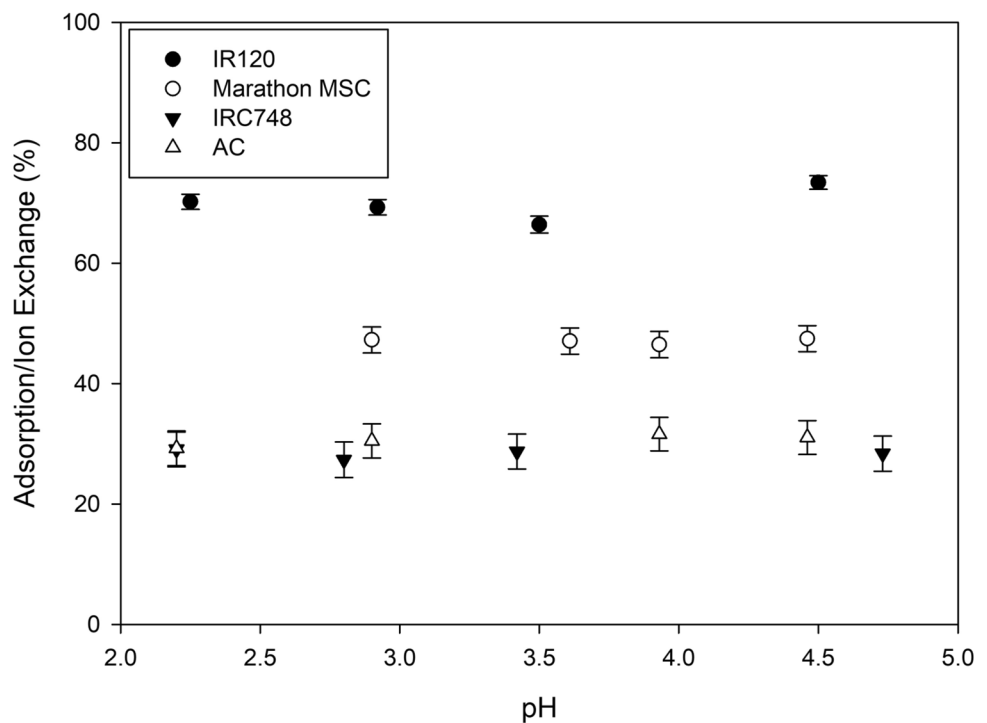
and the intraparticle diffusion controlled process (Amin et al. 2015; Dizge et al. 2009).

Effect of pH

Figure 9 shows the effect of pH on the amount of Ni^{2+} captured at equilibrium for the different adsorbents studied in this work. pH values between 2 and 5 were used to avoid metal precipitation. In this range, pH does not significantly affect the efficiency of Ni^{2+} adsorption/ion exchange for the adsorbents studied, except for the Amberlite IR120. For this latter resin, there was a slight influence of pH with a maximum ion exchange efficiency at pH = 4.5. This almost negligible influence of pH on ion exchange/adsorption could be due to the limited pH range used in our study. Indeed, at pH < 2, the presence of competing H$^+$ ions in solution and/or the protonation of the surface, particularly for AC, could lead to a strong repulsion between Ni^{2+} and the positively charged surface (Kobya et al. 2005) which would result in a reduction in the adsorption and exchange capacities of adsorbents. In addition, at pH > 5, there is a potential risk of precipitation of nickel ions due to the formation of nickel hydroxide (Alyüz and Veli 2009) which could therefore cause a decrease in adsorption/ion exchange capacity. In the literature, Demirbas et al. (2005) noticed a maximum recovery at pH values between 5 and 7. Rengaraj et al. (2002) and Alyüz and Veli (2009) observed no pH effect for the exchange of Ni^{2+} with other sulfonic acid resins (IRN77 and Dowex HCR S/S). On the contrary, Liu et al. (2014) found a pH effect for the exchange of Ni^{2+} with iminodiacetic acid resin. For the uptake of Ni^{2+} by AC,

Periasamy and Namasivayam (1995) and Kobya et al. (2005) demonstrated a pH effect on the adsorption. These somehow contradictory results seem to prove that the effect of pH on ion exchange/adsorption may be highly dependent on experimental conditions (e.g., initial concentration of Ni^{2+}, amount of adsorbent, type of nickel salt used).

Ion exchange/adsorption isotherms

The isotherms obtained for the three resins and AC are presented in Fig. 10. Under our experimental conditions, a Ni^{2+} concentration of 200 mg L^{-1} is enough to saturate all the accessible IRC748 ion exchange sites, i.e., the maximum capacity of this resin is reached. Whereas for the other adsorbents studied, a Ni^{2+} concentration of 800 mg L^{-1} is required. The data were analyzed with the Langmuir (Eq. 5) and Freundlich (Eq. 6) models, and the fittings are shown in Fig. 10. The obtained parameters and the correlation coefficients R^2 are listed in Table 5. The maximum adsorption capacity follows the order IRC748 > IR120 > Marathon MSC > AC. The Ni^{2+} ion-exchange/adsorption isotherm data follow the Langmuir model (Fig. 10). For the activated carbon and resins, q_{max} is close to the literature data (Amin et al. 2015; Khawaja et al. 2015; Mendes and Martins 2004) but the value of K_L differs sometimes by several orders of magnitude (Demirbas et al. 2005; Mendes and Martins 2004; Satapathy and Natarajan 2006). This can be explained by the diversity of AC preparations and activation protocols as well as by differences in experimental conditions, such
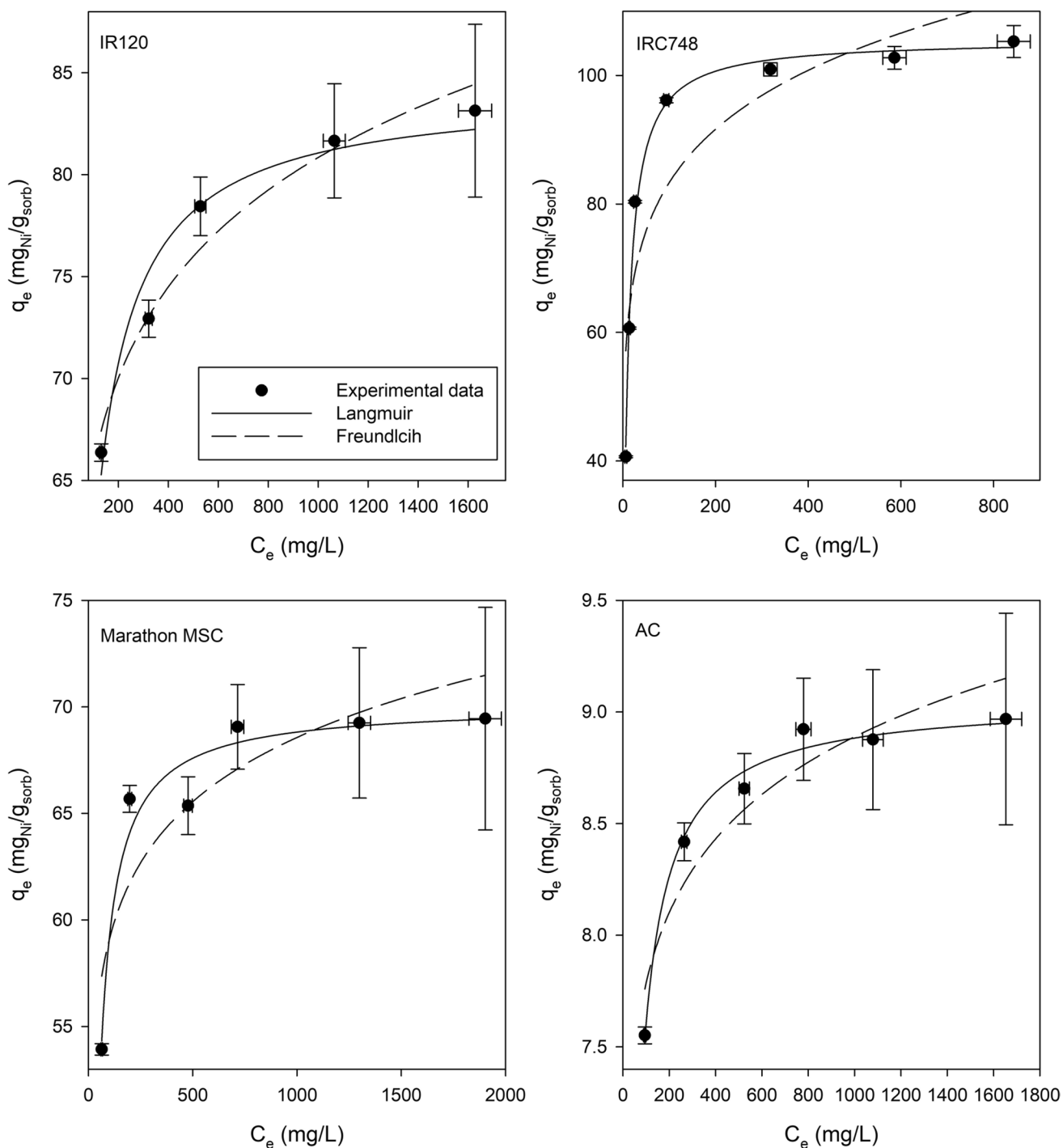
Fig. 10 Fitting of Freundlich and Langmuir isotherms for Ni^{2+} with resin/AC

as initial metal concentration, volume of the treated solution, amount of adsorbent, stirring speed, etc. Table 5 only reports the isotherm study analyzed with the Langmuir and Freundlich models, which, in our case, provide good correlation coefficients (especially the Langmuir model).

However, it should be mentioned that other models were also used in the literature to describe the ion exchange/adsorption isotherm of Ni^{2+} with resin/AC, such as Tempkin and Dubinin–Radushkevich models (Alyüz and Veli 2009; Amin et al. 2015; Patel 2020). Currently, only one

Table 5 Parameters of Langmuir and Freundlich model. Comparison with literature data

Adsorbent	T (°C)	pH	Langmuir q_{max} (mg$_{Ni}$/g$_{sorb}$)	K_L (L/mg$_{Ni}$)	R^2	Freundlich K_F (mg$_{Ni}^{1-1/n}$ g$_{sorb}^{-1}$ L$^{1/n}$)*	n	R^2	References
Activated charcoal	22	4.5	9.1 ± 0.1	$(5.22 \pm 0.31) \times 10^{-2}$	0.99	5.96 ± 0.38	17.3 ± 3.1	0.90	This study
Dowex Marathon MSC H + wet	22	4.5	70.1 ± 0.8	$(5.4 \pm 0.7) \times 10^{-2}$	0.96	43.8 ± 4.8	15.4 ± 4	0.90	This study
Amberlite IRC748 Na + wet	20	4.5	105.6 ± 1.1	6.01 ± 0.35	0.99	77.4 ± 4.8	7.3 ± 1.7	0.82	This study
Amberlite IR120 Na + wet	22	4.5	84.1 ± 1.2	$(2.64 \pm 0.37) \times 10^{-2}$	0.96	44 ± 3	11.2 ± 1.3	0.96	This study
Amberlite IR120 H + dry	20	/	48.1	29.7	/	235.3	1.2	/	Demirbas et al. (2005)
Amberlite IR120 H$^+$	45	/	16.6	10^{-2}	0.99	0.7	0.86	0.98	Fatima et al. (2020)
Dowex HCR S/S	23	4	156	2	/	68.5	4.38	/	Alyüz and Veli (2009)
Lewatit monoplus SP 112 H + dry	25	6	171	1.6	/	91.8	7.1	/	Dizge et al. (2009)
Amberlite IRN77 H +	25	/	/	/	/	81.8	5.9	/	Rengaraj et al. (2002)
Amberlite IRC748 H + wet	25	5	35.8	0.99	1.00	1.04	9.1	0.77	Zainol and Nicol (2009)
Chelating resin CR-10 Na + dry	25	4	164.9	6.47×10^{-3}	0.98	1.43	5.74	1.00	Dinu and Dragan (2008)
Amberlite IRC748 Na + dry	25	4.5	62.04	6.2×10^{-3}	0.99	/	/	/	Lin et al. (2008)
Lewatit CNP 80 H + dry	25	8	18.95	1.38×10^{-3}	0.99	/	/	/	Pehlivan and Altun (2007)
Amberlite IRC748 wet	25	3	125	1.22×10^{-3}	1.00	/	/	/	Mendes and Martins (2004)
Purolite C100-MB H + dry	20	5.5	70.06	2×10^{-3}	0.94	1.27	1.55	0.91	Amin et al. (2015)
Activated charcoal (neem leaf powder)	/	/	122.5	4.01×10^{-2}	0.99	7.12	0.4	0.98	Patel (2020)
Activated carbon (peanut hulls)	30	5	1.49	4×10^{-2}	1.00	/	/	/	Periasamy and Namasivayam (1995)
Activated carbon (Mespilus germanica leaves)	25	7	13.08	0.63	0.98	19.54	0.2	0.97	Khedri et al. (2022)
Granular activated carbon	25	5	2.9	1.8	0.98	0.25	4.18	0.97	Satapathy and Natarajan (2006)
Activated charcoal (pomegranate peel)	30	7	10.8	2.8×10^{-2}	0.94	0.45	1.47	0.93	Khawaja et al. (2015)
Granular activated carbon	/	/	29.8	1.2×10^{-2}	0.99	2	0.44	0.98	Rodríguez-Estupiñán et al. (2011)
Activated carbon	/	2	400	2×10^{-2}	0.78	11.1	0.4	0.99	Karnib et al. (2014)
Activated carbon (coconut shell)	25	5.8	83.16	5×10^{-3}	1.00	5.82	1.26	0.95	Moreno-Piraján et al. (2011)
Activated carbon (cassava tubers)	27	4	35.34	6.7×10^{-2}	0.97	8.56	3.41	0.93	Alongamo et al. (2021)
Activated carbon (bamboo)	/	5.5	61.35	1.34	1.00	1.02	35.46	1.00	Sivakumar et al. (2018)
Activated carbon (y Mangosteen shell)	/	/	57.14	9.3×10^{-2}	1.00	254.3	0.56	0.99	Anitha et al. (2021)

*Values were reported in the units indicated in the literature

paramagnetic ion is present in the studied solution. The addition of several paramagnetic ions would, of course, complicate the analysis. Indeed, in this case the measured relaxation time would reflect a global effect of the different paramagnetic ions in the system, which shows the limits of our method in terms of selectivity. Nevertheless, measurements at different magnetic fields could be carried out to observe the change in signal due to the variation in relaxivity of each paramagnetic ion. This aspect, as well as the study of heavy metal elimination in a real aquatic environment, will be addressed in the next stage of the project.

Relaxation induced by the Ni^{2+} loaded adsorbents

The results presented above were obtained by measuring the relaxation times of the solution (supernatant) and not directly on the adsorbent. However, the study of the adsorbent itself is a necessary step before setting up column experiments where the breakthrough curves of the sorbent could be followed in real time by NMR thanks to the relaxation properties of the loaded adsorbent. For this purpose, the relaxation properties of Ni^{2+} loaded resin/AC were studied.

Relaxation of the loaded resins

In the case of the resins, the obtained T_1 and T_2 relaxation curves present a biexponential behavior with slow- and fast-relaxing proton fractions. In this porous hydrated media, the slow-relaxing fraction can be related to water diffusing in the intergranular pores created by the packing of the adsorbent (interporosity). The fast-relaxing fraction is attributed to water present in the pores of the adsorbent (intraporosity). This interpretation was confirmed by centrifugation of the samples. Indeed, filtration by centrifugation allows the water present in the artificial intergranular pores and the water present in the porous media to be separated. Water in the intragranular porosity remains unaffected due to the high capillary potential of the pores. Grunewald and Knight (2009) already used centrifugation on Fe^{3+} doped silica gel to isolate the contribution of intragranular water: the initial bimodal T_2 distributions became unimodal after centrifugation. We obtained similar results with the Ni^{2+} loaded resins. The relaxation curves became monoexponential after centrifugation and the corresponding relaxation times were very close to those of the fast-relaxing fraction obtained for the wet resin without filtration (Table S5).

As resins have a broad pore size distribution with micro-, meso- and macropores (only for the macroporous resins),

one could expect several fractions for the intraporous water, corresponding to the different porosity types of the system. However, as mentioned above, we only observed a single fast fraction, corresponding to the entire pore network. This could be explained by a strong coupling between the different pores present in the media which results in a unique contribution from all the internal pores instead of many fractions corresponding to the different pore sizes in the media.

To extract information about the metal uptake by the resin, we decided to focus on this fast fraction, corresponding to water present inside the porous media. The relaxation rates of the fast-relaxing water fraction of the wet resin can be correlated with the metal content which was determined independently by ICP-AES/MS (Fig. 11). The data was fitted using an empirical equation:

$$1/T_i = a q_{ICP}^n + b \tag{9}$$

where $1/T_i$ is the relaxation rate of the fast fraction in 1/s and q_{ICP} is the actual metal content of the dry resin measured by ICP-AES/MS in mg_{Ni}/g_{sorb}. The fitting parameters obtained for the different resins are presented in Table S6.

The relaxation rates of the fast-relaxing water fraction of the Ni^{2+} loaded rehydrated IR120 and Marathon MSC resin clearly depend on the metal content. When the resin progressively captures paramagnetic Ni^{2+} ions, the surface relaxivity increases, which causes an increase of the relaxation rates (Fig. 11), as predicted by Eq. 8. Gossuin et al. (2020) already showed a correlation between the Cu^{2+} and Cr^{3+} loading of Amberlite IR120 with the relaxation times of the rehydrated resin. D'Agostino et al. (2017) also observed an increase in the relaxation times T_1, T_2 with the increase of Cu^{2+} impurities in porous alumina. The fast-relaxing water fractions obtained for the IR120 and Dowex resins do not show a linear relationship with the actual amount of captured Ni^{2+}, measured by ICP spectroscopy, which complicates the calculation of a detection limit. However, an attempt was made to estimate the limit of detection (LOD) by taking the initial four points of the T_2 curve and performing a linear fit. The T_2 fast fraction was chosen for the LOD because it presented the strongest relationship in the linear regression analysis, reflected by the highest R^2 value. Using the results of the fit, an estimate of the detection limit was derived using the expression proposed by the International Committee on Harmonization (ICH) (2005):

$$LOD = 3.3\sigma/m \tag{10}$$

where σ represents the residual standard deviation and m, the slope of the linear regression. A detection limit of 0.18 mg_{Ni}/g was obtained for the Dowex and 1.1 mg_{Ni}/g
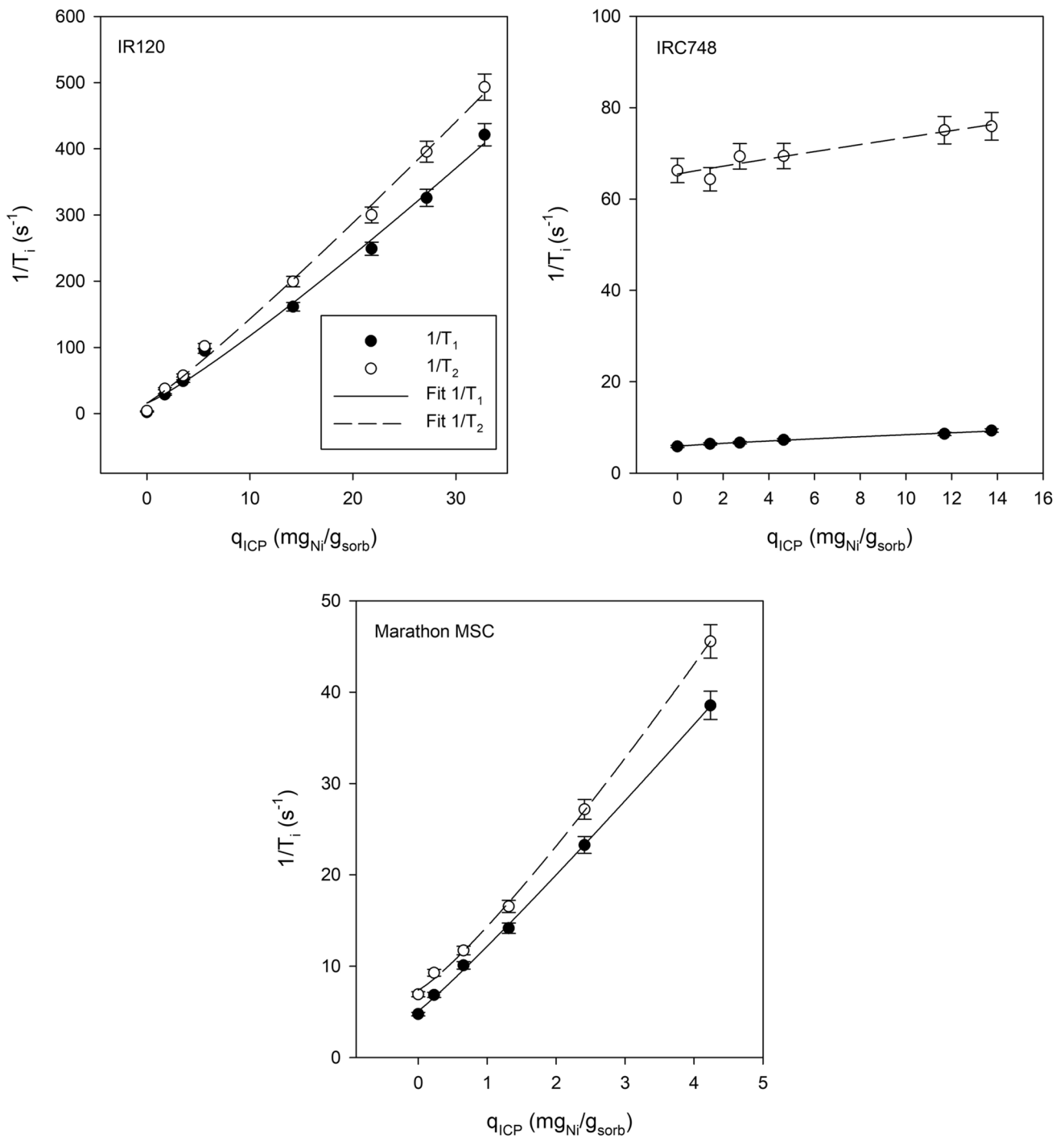
Fig. 11 Effect of Ni^{2+} content on the fast relaxation rates of the wet resin

for the IR120 resin. Although these values are significantly higher than the detection limits obtained by ICP-AES/MS spectroscopy, where values below 1 ppm were achieved, they are sufficient to follow the gradual loading of the sorbent with Ni^{2+}. Moreover, the main advantage of our technique does not reside in its sensitivity but in its ability to be used in situ to monitor column saturation in real time.

The iminodiacetic acid (IDA) resin IRC748 exhibits a different behavior to two sulfonic acid resins because of the chelating properties of its functional group. Indeed, Yuchi et al. (2002) demonstrated that the polymer complex of some divalent metal ions with an IDA chelating resin leads to a lower hydration number compared to hydrated metal ions. The same observation was made by Hoek and Reedijk (1979) who concluded that the IDA functional group coordinates as a tridentate chelating ligand to Ni^{2+}. Therefore, when a Ni^{2+} ion is captured by the IRC748 resin, the chelating group will complex the heavy metal, which leads to a reduction in the hydration number of the metal ion, thus significantly reducing the interaction between the Ni^{2+} and water protons. The effect of the content of captured Ni^{2+} on the relaxation properties of an IDA resin is thus less marked than for the two other resins, as illustrated in Fig. 11. The LOD obtained for the IRC748 was 7.3 mg_{Ni}/g, demonstrating the limitations of using NMR relaxometry for resins with chelating groups.

Relaxation of the loaded activated carbon

In contrast to the resins, activated carbon already contains paramagnetic impurities, which leads to an enhancement of surface relaxation before any adsorption. Moreover, the T_1 and T_2 relaxation curves of the studied AC present a multiexponential behavior with more than two fractions, which complicates the interpretation of the results. In order to eliminate one of the relaxing fractions, filtration by centrifugation was carried out on the Ni^{2+} loaded activated carbon samples. After draining water from the intergranular pores of the Ni^{2+} loaded AC with ultracentrifugation, we obtained biexponential relaxation curves with slow- and fast-relaxing proton fractions. Contrary to the case of resins, these two fractions are both related to water in the intragranular porosity. They correspond to two different porosity types present in the activated carbon. In this medium, the pore coupling seems to be weaker than in resin, which allows the differentiation of two pore sizes. Krutyeva et al. (2009) also observed the presence of two relaxing fractions in the T_2 relaxation curves of ethanol, nitrobenzene and toluene in activated carbon: a fast and a slow fraction, which they also attributed to the liquid confined in the micropores and to the liquid in the mesopores, respectively.

The slow and fast relaxing fractions obtained for the AC after centrifugation present the same qualitative evolution with the metal content, but the relaxation times of the fast fraction were so short that they became very difficult to measure accurately with conventional benchtop relaxometers (Fig. S4 and Fig. 12). Therefore, we decided to focus on the slow-relaxing fraction of the Ni^{2+} loaded AC after centrifugation, whose T_1 and T_2 are presented in Fig. 12. There is no significant change of the relaxation rates at low Ni^{2+} loading. An increase of $1/T_1$ and $1/T_2$ was only observed for loadings larger than 6.6 mg_{Ni}/g_{Ac}, for which there is a clear correlation between the relaxation rates and the AC Ni^{2+} content. This behavior is clearly different from what was observed for the resins (Fig. 11).
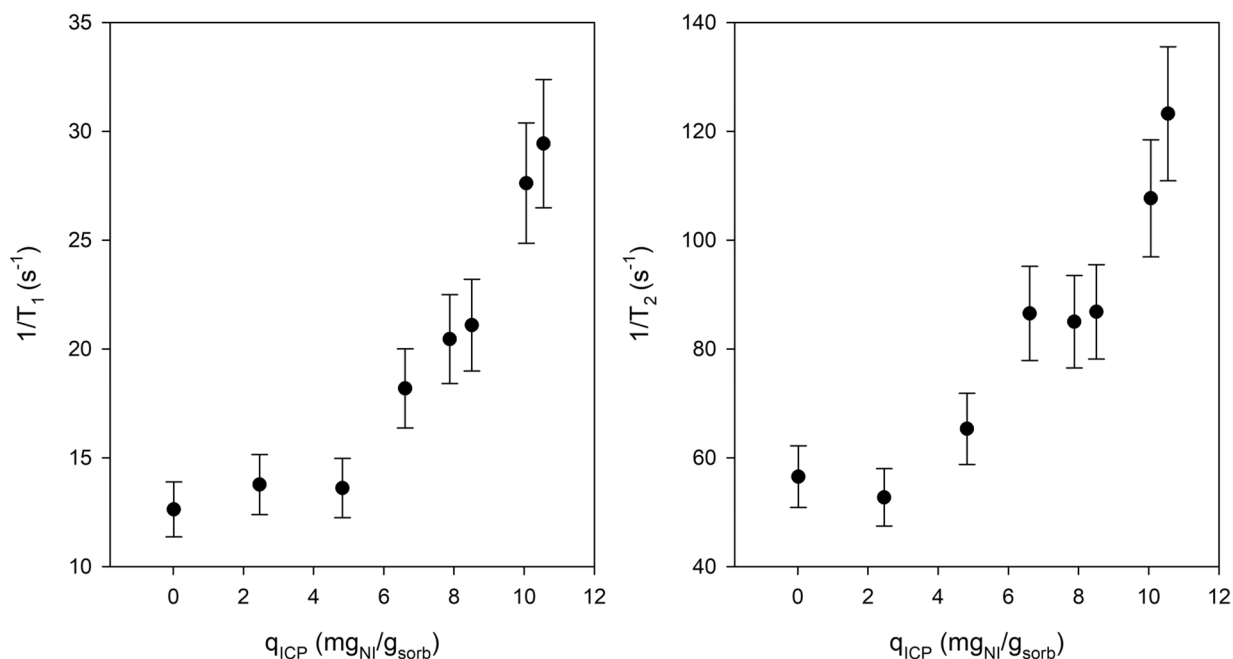

Fig. 12 Effect of Ni^{2+} content on the slow relaxation rates of the activated carbon after filtration by centrifugation

A first explanation for this lack of initial dependence between the relaxation time and the AC Ni^{2+} loading could be the initial saturation of micropores with Ni^{2+} ions. These ions would be invisible from the NMR point of view because the relaxation of water contained in these micropores is too fast. Indeed, the large surface to volume ratio associated to the micropores leads to small relaxation times (Eq. 7). In this case, Ni^{2+} ions would only start to influence the relaxation rates of the slow fraction once all the micropores sites are occupied.

Another reason for this lack of initial dependence between the relaxation time and the AC Ni^{2+} loading could be given by the formation of complexes between Ni^{2+} and possible functional groups present on the surface of activated carbon. The oxygen surface groups of functionalized activated carbon show a strong affinity for heavy metal ions, forming complexes (Chen and Wu 2004; Xiao and Thomas 2004; Yang et al. 2019). Therefore, Ni^{2+} could react preferentially with these surface groups, including carboxylic groups, saturating them before penetrating the inner porosity of the activated carbon. In this interpretation, complexation of Ni^{2+} would be observed up to 6 mg g^{-1}, after which all accessible carboxyl groups would be saturated and only Ni^{2+} adsorption into the AC pores would be possible. The complexes formed between the oxygenated functional groups and Ni^{2+} proved to be diamagnetic. Indeed, according to crystal field theory, the oxygenated carboxylic complex can induce a low-spin nickel complex with a reduction in the number of unpaired electrons from 2 to 0, resulting in a zero magnetic moment. Such a low-spin nickel complex would be invisible to NMR relaxometry. This magnetic behavior aligns with the findings of Bala et al. (2007), who demonstrated a loss of magnetism in Ni^{2+} complexes with carboxyl groups, however, their DFT calculations did not take into account the potential presence of third-party ligands such as water. Bhatnagar et al. (1928) also reported a loss of paramagnetism of the nickel salt after adsorption on charcoal, which they also attributed to the formation of a covalent complex between the Ni^{2+} and the charcoal surface. Although XPS analysis did not reveal the presence of low-spin nickel complexes; additional measurements with Electron Paramagnetic Resonance might help to determine whether these low-spin complexes are present or not.

From Eq. 8, the transverse and longitudinal surface relaxivities were estimated for each of the carbon samples using the slow relaxing part of the relaxation time and the independent measurement of S/V by BJH analysis. Previously, we assumed that the two relaxing fractions obtained were related to different porosities: the fast one can be related to the smallest pores (microporosity) and the slow one is linked to bigger pores (mesoporosity). Therefore, we used the surface area of the mesopores and the mesopore volume, obtained by N_2 adsorption isotherm and the BJH model from Table 3, to calculate the S/V ratio. The calculated surface relaxivities can be found in Table S7. The surface relaxivities of AC increase with the Ni^{2+} content. Indeed, the transverse surface relaxivity increases from 0.128 to 0.258 μm s^{-1} between the unloaded sample and sample with the maximal Ni^{2+} content. Horch et al. (2014) estimated the transverse surface relaxivity of methane-saturated activated carbon at 0.05 μm s^{-1}. To our knowledge, no other studies have been carried out on surface relaxivities of activated carbon. However, the values obtained in this work can be compared to the literature data for other porous media doped or not with paramagnetic impurities. The magnitude of the surface relaxation found is of the order of 10^{-3}–100 μm s^{-1} (Bryar et al. 2000; Foley et al. 1996; Keating and Knight 2007; Saidian and Prasad 2015). Surface relaxivities clearly depend on the studied media, its magnetic properties as well as on the concentration of paramagnetic impurities.

In any case, the correlation between the relaxation rates and the metal content of all the adsorbents is promising in the perspective of the in situ study, by NMR relaxometry, of resin/carbon loading during a column experiment. Of course, when compared to AES spectroscopy, the sensitivity of the NMR relaxometry technique is lower, but it also presents advantages: it is nondestructive and can be directly performed on the column, and it is fast enough to follow the loading of the resin/AC in real time, which we will show in a forthcoming study.

Conclusion

In this work, we harnessed the power of NMR relaxometry to investigate the Ni^{2+} ion exchange and adsorption processes, using a range of cationic resins (Amberlite IR120, Dowex Marathon MSC, and Amberlite IRC748) and a commercial activated carbon in batch experiments. This allowed us to determine the ion exchange/adsorption rates as well as the maximum Ni^{2+} removal capacity of the resins and AC. The influence of molecules that could form complexes with the paramagnetic ions, as well as the study of heavy metal elimination in a real aquatic environment, will also be addressed in the next stage of the project. However, this preliminary study demonstrates the ability of NMR to track changes in the relaxation times of a solution during the depollution process. More importantly, the study of the relaxation properties of loaded sorbents not only demonstrates the versatility of NMR relaxometry,

but also highlights its potential for real-time monitoring of breakthrough curves in column experiments, which is not feasible with the ICP spectroscopy method. The next step of this project will be to capture, in real time, changes in the relaxation properties of the adsorbent and the solution throughout the metal loading process.

Declarations

Conflict of interest The authors declare that they have no known competing financial interests or personal relationships that could have appeared to influence the work reported in this paper.

References

Akpor OB (2014) Heavy metal pollutants in wastewater effluents: sources, effects and remediation. ABB 2:37. https://doi.org/10.11648/j.abb.20140204.11

Alguacil FJ (2017) La eliminación de metales tóxicos presentes en efluentes líquidos mediante resinas de cambio iónico. Parte V: níquel(II))/H+/Dowex C400. Revmetal 53:105. https://doi.org/10.3989/revmetalm.105

Alongamo BAA, Ajifack LD, Ghogomu JN, Nsami NJ, Ketcha JM (2021) Activated carbon from the peelings of cassava tubers (*Manihot esculenta*) for the removal of nickel(II) ions from aqueous solution. J Chem 2021:1–14. https://doi.org/10.1155/2021/5545110

Alyüz B, Veli S (2009) Kinetics and equilibrium studies for the removal of nickel and zinc from aqueous solutions by ion exchange resins. J Hazard Mater 167:482–488. https://doi.org/10.1016/j.jhazmat.2009.01.006

Amin NK, Abdelwahab O, El-Ashtoukhy E-SZ (2015) Removal of Cu(II) and Ni(II) by ion exchange resin in packed rotating cylinder. Desalin Water Treat 55:199–209. https://doi.org/10.1080/19443994.2014.913208

Anitha D, Ramadevi A, Seetharaman R (2021) Biosorptive removal of Nickel(II) from aqueous solution by Mangosteen shell activated carbon. Mater Today Proc 45:718–722. https://doi.org/10.1016/j.matpr.2020.02.748

Ates N, Basak A (2021) Selective removal of aluminum, nickel and chromium ions by polymeric resins and natural zeolite from anodic plating wastewater. Int J Environ Health Res 31:102–119. https://doi.org/10.1080/09603123.2019.1631263

Azeh Engwa G, Udoka Ferdinand P, Nweke Nwalo F, Unachukwu MN (2019) Mechanism and health effects of heavy metal toxicity in humans. In: Karcioglu O, Arslan B (eds) Poisoning in the modern world—new tricks for an old dog? IntechOpen, Rijeka. https://doi.org/10.5772/intechopen.82511

Bala T, Prasad BLV, Sastry M, Kahaly MU, Waghmare UV (2007) Interaction of different metal ions with carboxylic acid group: a quantitative study. J Phys Chem A 111:6183–6190. https://doi.org/10.1021/jp067906x

Bartacek J, Vergeldt FJ, Maca J, Gerkema E, Van As H, Lens PNL (2016) Iron, cobalt, and gadolinium transport in methanogenic granules measured by 3D magnetic resonance imaging. Front Environ Sci 4:13. https://doi.org/10.3389/fenvs.2016.00013

Beamson G, Briggs D (2000) The XPS of polymers database, version 1.0. SurfaceSpectra, Manchester

Bertini I, Luchinat C, Parigi G (2005) 1H NMRD profiles of paramagnetic complexes and metalloproteins. Adv Inorg Chem 57:105–172. https://doi.org/10.1016/S0898-8838(05)57003-X

Bhatnagar SS, Mathur KN, Kapur PL (1928) Magnetic properties of some substances in the adsorbed state. Indian J Phys 3:53

Biesinger MC, Payne BP, Lau LWM, Gerson A, Smart R, St C (2009) X-ray photoelectron spectroscopic chemical state quantification of mixed nickel metal, oxide and hydroxide systems. Surf Interface Anal 41:324–332. https://doi.org/10.1002/sia.3026

Biesinger MC, Lau LWM, Gerson AR, Smart R, St C (2012) The role of the Auger parameter in XPS studies of nickel metal, halides and oxides. Phys Chem Chem Phys 14:2434. https://doi.org/10.1039/c2cp22419d

Briffa J, Sinagra E, Blundell R (2020) Heavy metal pollution in the environment and their toxicological effects on humans. Heliyon 6:e04691. https://doi.org/10.1016/j.heliyon.2020.e04691

Brownstein KR, Tarr CE (1979) Importance of classical diffusion in NMR studies of water in biological cells. Phys Rev A 19:2446–2453. https://doi.org/10.1103/PhysRevA.19.2446

Bryar TR, Daughney CJ, Knight RJ (2000) Paramagnetic effects of Iron(III) species on nuclear magnetic relaxation of fluid protons in porous media. J Magn Resonan 142:74–85. https://doi.org/10.1006/jmre.1999.1917

Burakov AE, Galunin EV, Burakova IV, Kucherova AE, Agarwal S, Tkachev AG, Gupta VK (2018) Adsorption of heavy metals on conventional and nanostructured materials for wastewater treatment purposes: a review. Ecotoxicol Environ Saf 148:702–712. https://doi.org/10.1016/j.ecoenv.2017.11.034

Charerntanyarak L (1999) Heavy metals removal by chemical coagulation and precipitation. Water Sci Technol 39:135–138. https://doi.org/10.1016/S0273-1223(99)00304-2

Chen JP, Wu S (2004) Acid/base-treated activated carbons: characterization of functional groups and metal adsorptive properties. Langmuir 20:2233–2242. https://doi.org/10.1021/la0348463

D'Agostino C, Bräuer P, Charoen-Rajapark P, Crouch MD, Gladden LF (2017) Effect of paramagnetic species on T_1, T_2 and T_1/T_2 NMR relaxation times of liquids in porous $CuSO_4/Al_2O_3$. RSC Adv 7:36163–36167. https://doi.org/10.1039/C7RA07165E

Demirbas A, Pehlivan E, Gode F, Altun T, Arslan G (2005) Adsorption of Cu(II), Zn(II), Ni(II), Pb(II), and Cd(II) from aqueous solution on Amberlite IR-120 synthetic resin. J Colloid Interface Sci 282:20–25. https://doi.org/10.1016/j.jcis.2004.08.147

Dinu MV, Dragan ES (2008) Heavy metals adsorption on some iminodiacetate chelating resins as a function of the adsorption parameters. React Funct Polym 68:1346–1354. https://doi.org/10.1016/j.reactfunctpolym.2008.06.011

Dizge N, Keskinler B, Barlas H (2009) Sorption of Ni(II) ions from aqueous solution by Lewatit cation-exchange resin. J Hazard Mater 167:915–926. https://doi.org/10.1016/j.jhazmat.2009.01.073

Edwards HGM, Brown DR, Dale JA, Plant S (2000) Raman spectroscopy of sulfonated polystyrene resins. Vib Spectrosc 24:213–224. https://doi.org/10.1016/S0924-2031(00)00070-9

El-Hamid AMA, Zahran MA, Ahmed YMZ, El-Sheikh SM (2020) Separation of heavy metal ions from petroleum ash liquor using organic resins and FT-IR study of the process. Radiochemistry 62:243–250. https://doi.org/10.1134/S1066362220020125

Fatima N, Zhang Q, Chen R, Yan D, Zhou Q, Lu X, Xin J (2020) Adsorption thermodynamics and kinetics of resin for metal impurities in bis(2-hydroxyethyl) terephthalate. Polymers 12:2866. https://doi.org/10.3390/polym12122866

Foley I, Farooqui SA, Kleinberg RL (1996) Effect of paramagnetic ions on NMR relaxation of fluids at solid surfaces. J Magn Resonan Ser A 123:95–104. https://doi.org/10.1006/jmra.1996.0218

Gautam RK, Jaiswal A, Chattopadhyaya MC (2014) Functionalized magnetic nanoparticles for heavy metal removal from aqueous solutions: kinetics and equilibrium modeling. In: Tiwari A, Syväjärvi M (eds) Advanced materials for agriculture, food, and environmental safety. Wiley, Hoboken, pp 291–331. https://doi.org/10.1002/9781118773857.ch11

Gossuin Y, Vuong QL (2018) NMR relaxometry for adsorption studies: proof of concept with copper adsorption on activated alumina. Sep Purif Technol 202:138–143. https://doi.org/10.1016/j.seppur.2018.03.051

Gossuin Y, Hantson A-L, Vuong QL (2020) Low resolution benchtop nuclear magnetic resonance for the follow-up of the removal of Cu^{2+} and Cr^{3+} from water by amberlite IR120 ion exchange resin. J Water Process Eng 33:101024. https://doi.org/10.1016/j.jwpe.2019.101024

Goyer RA, Clarkson TW (1996) Toxic effects of metals. In: Klaassen CD (ed) The basic science of poisons, 5th edn. McGraw-Hill Health Professions Division, New York, pp 813–858

Grunewald E, Knight R (2009) A laboratory study of NMR relaxation times and pore coupling in heterogeneous media. Geophysics 74:E215–E221. https://doi.org/10.1190/1.3223712

Gupta RP, Sen SK (1975) Calculation of multiplet structure of core p-vacancy levels II. Phys Rev B 12:15–19. https://doi.org/10.1103/PhysRevB.12.15

He ZL, Yang XE, Stoffella PJ (2005) Trace elements in agroecosystems and impacts on the environment. J Trace Elem Med Biol 19:125–140. https://doi.org/10.1016/j.jtemb.2005.02.010

Ho YS, McKay G (1998) Sorption of dye from aqueous solution by peat. Chem Eng J 70:115–124. https://doi.org/10.1016/S0923-0467(98)00076-1

Hoek PJ, Reedijk J (1979) Coordination of transition-metal ions by chelating cation-exchange resins; Co(II), Ni(II) and Cu(II) coordinated by the iminodiacetate group in Chelex-100. J Inorg Nucl Chem 41:401–404. https://doi.org/10.1016/0022-1902(79)80154-2

Horch C, Schlayer S, Stallmach F (2014) High-pressure low-field 1H NMR relaxometry in nanoporous materials. J Magn Reson 240:24–33. https://doi.org/10.1016/j.jmr.2014.01.002

Jha MK, Van Nguyen N, Lee J, Jeong J, Yoo J-M (2009) Adsorption of copper from the sulphate solution of low copper contents using the cationic resin Amberlite IR 120. J Hazard Mater 164:948–953. https://doi.org/10.1016/j.jhazmat.2008.08.103

Kalak T, Cierpiszewski R, Ulewicz M (2021) High efficiency of the removal process of Pb(II) and Cu(II) ions with the use of fly ash from incineration of sunflower and wood waste using the CFBC technology. Energies 14:1771. https://doi.org/10.3390/en14061771

Karnib M, Kabbani A, Holail H, Olama Z (2014) Heavy metals removal using activated carbon, silica and silica activated carbon composite. Energy Procedia 50:113–120. https://doi.org/10.1016/j.egypro.2014.06.014

Katz S, Pevzner A, Shepelev V, Marx S, Rotter H, Amitay-Rosen T, Nir I (2022) Activated carbon aging processes characterization by Raman spectroscopy. MRS Adv 7:245–248. https://doi.org/10.1557/s43580-021-00189-9

Keating K, Knight R (2007) A laboratory study to determine the effect of iron oxides on proton NMR measurements. Geophysics 72:E27–E32. https://doi.org/10.1190/1.2399445

Khawaja M, Mubarak S, Zia-Ur-Rehman M, Kazi AA, Hamid A (2015) Adsorption studies of pomegranate peel activated charcoal for nickel(II) ion. J Chil Chem Soc 60:2642–2645. https://doi.org/10.4067/S0717-97072015000400003

Khedri A, Jafari D, Esfandyari M (2022) Adsorption of Nickel(II) ions from synthetic wastewater using activated carbon prepared from *Mespilus germanica* leaf. Arab J Sci Eng 47:6155–6166. https://doi.org/10.1007/s13369-021-06014-7

Kobya M, Demirbas E, Senturk E, Ince M (2005) Adsorption of heavy metal ions from aqueous solutions by activated carbon prepared from apricot stone. Bioresour Technol 96:1518–1521. https://doi.org/10.1016/j.biortech.2004.12.005

Kock F, Colnago L (2022) NMR relaxometry applied to chemical studies of paramagnetic metal cation complexes: fundamentals and applications. J Braz Chem Soc. https://doi.org/10.21577/0103-5053.20220045

Kock FVC, Machado MP, Athayde GPB, Colnago LA, Barbosa LL (2018) Quantification of paramagnetic ions in solution using time domain NMR. PROS and CONS to optical emission spectrometry method. Microchem J 137:204–207. https://doi.org/10.1016/j.microc.2017.10.013

Kołodyńska D, Fila D, Hubicki Z (2020) Static and dynamic studies of lanthanum(III) ion adsorption/desorption from acidic solutions using chelating ion exchangers with different functionalities. Environ Res 191:110171. https://doi.org/10.1016/j.envres.2020.110171

Krutyeva M, Grinberg F, Furtado F, Galvosas P, Kärger J, Silvestre-Albero A, Sepulveda-Escribano A, Silvestre-Albero J, Rodríguez-Reinoso F (2009) Characterization of carbon materials with the help of NMR methods. Microporous Mesoporous

Mater 120:91–97. https://doi.org/10.1016/j.micromeso.2008.12.016

Larkin P (2011) Infrared and Raman spectroscopy: principles and spectral interpretation. Elsevier, Amsterdam

Lata H, Garg VK, Gupta RK (2008) Sequestration of nickel from aqueous solution onto activated carbon prepared from *Parthenium hysterophorus* L. J Hazard Mater 157:503–509. https://doi.org/10.1016/j.jhazmat.2008.01.011

Lin L-C, Li J-K, Juang R-S (2008) Removal of Cu(II) and Ni(II) from aqueous solutions using batch and fixed-bed ion exchange processes. Desalination 225:249–259. https://doi.org/10.1016/j.desal.2007.03.017

Ling P, Liu F, Li L, Jing X, Yin B, Chen K, Li A (2010) Adsorption of divalent heavy metal ions onto IDA-chelating resins: simulation of physicochemical structures and elucidation of interaction mechanisms. Talanta 81:424–432. https://doi.org/10.1016/j.talanta.2009.12.019

Liu Y, Li X, Wang C, Kong X, Zhoug L (2014) Poly(styrene-co-divinylbenzene)-PAMAM-IDA chelating resin: synthesis, characterization and application for Ni(II) removal in aqueous. J Cent South Univ 21:3479–3484. https://doi.org/10.1007/s11771-014-2325-5

Lowell S, Shields JE, Thomas MA, Thommes M (2004) Adsorption mechanism. In: Lowell S, Shields JE, Thomas MA, Thommes M (eds) Characterization of porous solids and powders: surface area, pore size and density, particle technology series. Springer, Dordrecht, pp 15–57. https://doi.org/10.1007/978-1-4020-2303-3_4

Mendes FD, Martins AH (2004) Selective sorption of nickel and cobalt from sulphate solutions using chelating resins. Int J Miner Process 74:359–371. https://doi.org/10.1016/j.minpro.2004.04.003

Michal CA (2020) Low-cost low-field NMR and MRI: instrumentation and applications. J Magn Reson 319:106800. https://doi.org/10.1016/j.jmr.2020.106800

Moradi AB, Oswald SE, Massner JA, Pruessmann KP, Robinson BH, Schulin R (2008) Magnetic resonance imaging methods to reveal the real-time distribution of nickel in porous media. Eur J Soil Sci 59:476–485. https://doi.org/10.1111/j.1365-2389.2007.00999.x

Moreno-Piraján JC, Garcia-Cuello VS, Giraldo L (2011) The removal and kinetic study of Mn, Fe, Ni and Cu ions from wastewater onto activated carbon from coconut shells. Adsorption 17:505–514. https://doi.org/10.1007/s10450-010-9311-5

Nestle N, Baumann T, Wunderlich A, Niessner R (2003) MRI observation of heavy metal transport in aquifer matrices down to sub-mg quantities. Magn Reson Imaging 21:345–349. https://doi.org/10.1016/S0730-725X(03)00166-8

Park SH, McClain S, Tian ZR, Suib SL, Karwacki C (1997) Surface and bulk measurements of metals deposited on activated carbon. Chem Mater 9:176–183. https://doi.org/10.1021/cm9602712

Patel H (2020) Batch and continuous fixed bed adsorption of heavy metals removal using activated charcoal from neem (*Azadirachta indica*) leaf powder. Sci Rep 10:16895. https://doi.org/10.1038/s41598-020-72583-6

Pehlivan E, Altun T (2007) Ion-exchange of Pb^{2+}, Cu^{2+}, Zn^{2+}, Cd^{2+}, and Ni^{2+} ions from aqueous solution by Lewatit CNP 80. J Hazard Mater 140:299–307. https://doi.org/10.1016/j.jhazmat.2006.09.011

Periasamy K, Namasivayam C (1995) Removal of nickel(II) from aqueous solution and nickel plating industry wastewater using an agricultural waste: Peanut hulls. Waste Manag 15:63–68. https://doi.org/10.1016/0956-053X(94)00071-S

Qasem NAA, Mohammed RH, Lawal DU (2021) Removal of heavy metal ions from wastewater: a comprehensive and critical review. NPJ Clean Water 4:36. https://doi.org/10.1038/s41545-021-00127-0

Rajendran S, Priya AK, Senthil Kumar P, Hoang TKA, Sekar K, Chong KY, Khoo KS, Ng HS, Show PL (2022) A critical and recent developments on adsorption technique for removal of heavy metals from wastewater-a review. Chemosphere 303:135146. https://doi.org/10.1016/j.chemosphere.2022.135146

Rengaraj S, Yeon K-H, Kang S-Y, Lee J-U, Kim K-W, Moon S-H (2002) Studies on adsorptive removal of Co(II), Cr(III) and Ni(II) by IRN77 cation-exchange resin. J Hazard Mater 92:185–198. https://doi.org/10.1016/S0304-3894(02)00018-3

Rodríguez-Estupiñán P, Giraldo L, Moreno-Piraján JC (2011) Nickel(II) ion adsorption onto activated carbon. Relationship between physicochemical properties and adsorption capacity. Adsorpt Sci Technol 29:541–551. https://doi.org/10.1260/0263-6174.29.6.541

Saidian M, Prasad M (2015) Effect of mineralogy on nuclear magnetic resonance surface relaxivity: a case study of Middle Bakken and Three Forks formations. Fuel 161:197–206. https://doi.org/10.1016/j.fuel.2015.08.014

Satapathy D, Natarajan GS (2006) Potassium bromate modification of the granular activated carbon and its effect on nickel adsorption. Adsorption 12:147–154. https://doi.org/10.1007/s10450-006-0376-0

Seah MP (1995) A system for the intensity calibration of electron spectrometers. J Electron Spectro Relat Phenom 71:191–204. https://doi.org/10.1016/0368-2048(94)02275-5

Seah MP (2012) Simple universal curve for the energy-dependent electron attenuation length for all materials. Surf Interface Anal 44:1353–1359. https://doi.org/10.1002/sia.5033

Sharma SK (ed) (2014) Heavy metals in water: presence, removal and safety. Royal Society of Chemistry, Cambridge

Shin S, Jang J, Yoon S-H, Mochida I (1997) A study on the effect of heat treatment on functional groups of pitch based activated carbon fiber using FTIR. Carbon 35:1739–1743. https://doi.org/10.1016/S0008-6223(97)00132-2

Silva RA, Hawboldt K, Zhang Y (2018) Application of resins with functional groups in the separation of metal ions/species—a review. Miner Process Extract Metall Rev 39:395–413. https://doi.org/10.1080/08827508.2018.1459619

Sivakumar D, Nouri J, Modhini TM, Deepalakshmi K (2018) Nickel removal from electroplating industry wastewater: a bamboo activated carbon. Glob J Environ Sci Manag 4:325–338

Tchounwou PB, Yedjou CG, Patlolla AK, Sutton DJ (2012) Heavy metal toxicity and the environment. In: Luch A (ed) Molecular, clinical and environmental toxicology, experientia supplementum. Springer, Basel, pp 133–164. https://doi.org/10.1007/978-3-7643-8340-4_6

Thapliyal V, Alabdulkarim ME, Whelan DR, Mainali B, Maxwell JL (2022) A concise review of the Raman spectra of carbon allotropes. Diamond Relat Mater 127:109180. https://doi.org/10.1016/j.diamond.2022.109180

The International Committee on Harmonization (ICH) (2005) Validation of analytical procedures: text and methodology. Q2(R1)

Thommes M, Kaneko K, Neimark AV, Olivier JP, Rodriguez-Reinoso F, Rouquerol J, Sing KSW (2015) Physisorption of gases, with special reference to the evaluation of surface area and pore size distribution (IUPAC technical report). Pure Appl Chem 87:1051–1069. https://doi.org/10.1515/pac-2014-1117

Vijayan N, Rani N, Madhurambal G, Bhagavannarayana G, Rathi B, Philip R, Safakath K, Mojumdar SC (2013) Synthesis, growth, and characterization of iminodiacetic acid monohydrochloride: a semi-organic single crystal for optical limiting applications. J Therm Anal Calorim 112:1113–1119. https://doi.org/10.1007/s10973-013-3041-3

Wang G, Li A, Li M (2010) Sorption of nickel ions from aqueous solutions using activated carbon derived from walnut shell waste.

Desalin Water Treat 16:282–289. https://doi.org/10.5004/dwt.2010.1863

Wołowicz A, Wawrzkiewicz M (2021) Screening of ion exchange resins for hazardous Ni(II) removal from aqueous solutions: kinetic and equilibrium batch adsorption method. Processes 9:285. https://doi.org/10.3390/pr9020285

Xiao B, Thomas KM (2004) Competitive adsorption of aqueous metal ions on an oxidized nanoporous activated carbon. Langmuir 20:4566–4578. https://doi.org/10.1021/la049712j

Yakout SM, Sharaf El-Deen G (2016) Characterization of activated carbon prepared by phosphoric acid activation of olive stones. Arab J Chem 9:S1155–S1162. https://doi.org/10.1016/j.arabjc.2011.12.002

Yang X, Wan Y, Zheng Y, He F, Yu Z, Huang J, Wang H, Ok YS, Jiang Y, Gao B (2019) Surface functional groups of carbon-based adsorbents and their roles in the removal of heavy metals from aqueous solutions: a critical review. Chem Eng J 366:608–621. https://doi.org/10.1016/j.cej.2019.02.119

Yin C, Aroua M, Daud W (2007) Review of modifications of activated carbon for enhancing contaminant uptakes from aqueous solutions. Sep Purif Technol 52:403–415. https://doi.org/10.1016/j.seppur.2006.06.009

Yuchi A, Sotomura Y, Ueda K (2002) Hydration of polymer complexes with iminodiacetate-type chelating resin. BCSJ 75:731–734. https://doi.org/10.1246/bcsj.75.731

Zainol Z, Nicol MJ (2009) Ion-exchange equilibria of Ni^{2+}, Co^{2+}, Mn^{2+} and Mg^{2+} with iminodiacetic acid chelating resin Amberlite IRC 748. Hydrometallurgy 99:175–180. https://doi.org/10.1016/j.hydromet.2009.08.004

Zamora-Ledezma C, Negrete-Bolagay D, Figueroa F, Zamora-Ledezma E, Ni M, Alexis F, Guerrero VH (2021) Heavy metal water pollution: a fresh look about hazards, novel and conventional remediation methods. Environ Technol Innov 22:101504. https://doi.org/10.1016/j.eti.2021.101504